RESEARCH ARTICLE

Key Points:
- Simulated Atlantic δ^{13}C reflects large-scale deep-ocean circulation patterns
- Flow speeds (SS) reflect local changes in vertical water mass characteristics
- Combining δ^{13}C and SS yields complementary information on AMOC changes

Supporting Information:
- Readme
- Table S1
- Table S2
- Table S3

Correspondence to:
P. Bakker,
pbakker@coas.oregonstate.edu

The evolution of deep-ocean flow speeds and δ¹³C under large changes in the Atlantic overturning circulation: Toward a more direct model-data comparison

Pepijn Bakker[1,2], **Aline Govin**[3,4], **David J. R. Thornalley**[5], **Didier M. Roche**[1,6], **and Hans Renssen**[1]

[1]Faculty of Earth and Life Sciences, VU University Amsterdam, Amsterdam, Netherlands, [2]Now at College of Earth, Ocean and Atmospheric Sciences, Oregon State University, Corvallis, Oregon, USA, [3]MARUM-Center for Marine Environmental Sciences, University of Bremen, Bremen, Germany, [4]Now at Institut Pierre-Simon Laplace/Laboratoire des Sciences du Climat et de l'Environnement, UMR 8212, CEA-CNRS-UVSQ, Gif-sur-Yvette, France, [5]Department of Geography, University College London, London, UK, [6]Laboratoire des Sciences du Climat et de l'Environnement, Gif-sur-Yvette, France

Abstract To investigate the dynamics of the Atlantic meridional overturning circulation (AMOC) on timescales longer than the observational records, model-data comparisons of past AMOC variability are imperative. However, this remains challenging because of dissimilarities between different proxy-based AMOC tracers and the difficulty of comparing these to model output. We present an *i*LOVECLIM simulation with tuned AMOC evolution and focus on AMOC tracers that are directly comparable to reconstructions: flow speeds and δ^{13}C. We deduce their driving factors and show that they yield different but complementary information about AMOC changes. Simulated flow speed changes are only linked to AMOC changes in regions bathed by North Atlantic Deep Water; however, in those regions they do provide details on vertical migration and thickness changes of the water masses. Simulated δ^{13}C changes in the North Atlantic Deep Water region are again related to AMOC changes. Yet in regions bathed by Antarctic Bottom Water or Antarctic Intermediate Water, the δ^{13}C evolution is driven by Southern Hemisphere source water δ^{13}C changes, while in the Nordic Seas and the two major overflow regions it is driven by Northern Hemisphere source water δ^{13}C changes. This shows that AMOC changes are not necessarily recorded by δ^{13}C and stresses the need for combining both tracers in paleoclimate studies. A preliminary model-data comparison for Last Interglacial flow speeds and δ^{13}C changes in the Deep Western Boundary Current shows that this integrated approach is far from straightforward and currently inconclusive on the Last Interglacial AMOC evolution. Nonetheless, the approach yields potential for more direct and in-depth model-data comparisons of past AMOC changes.

1. Introduction

Many paleoclimatic records indicate that the strength of the Atlantic meridional overturning circulation (AMOC) fluctuated on centennial to multimillennial timescales during present and past interglacials. Examples of such fluctuations are found during the early part of the present interglacial, the so-called 8.2 event [*Alley et al.*, 1997; *Ellison et al.*, 2006; *Kleiven et al.*, 2008], and during the early part of the Last Interglacial [*Oppo et al.*, 1997, 2006; *Hodell et al.*, 2009; *Sánchez Goñi et al.*, 2012; *Govin et al.*, 2012; *Galaasen et al.*, 2014]. Investigating the variability and stability of the AMOC during past warm periods is highly relevant in the light of predicted climate warming [*Solomon et al.*, 2007]. However, interpreting the body of proxy-based paleoclimatic evidence and tying this in with findings from climate model experiments is far from straightforward. Here we present modeling results that aim to identify the factors controlling the Last Interglacial evolution of two important variables used in proxy-based studies of AMOC variability, flow speed and δ^{13}C, with a particular focus on their similarities and differences.

The AMOC is a concept that describes a wind- and density-driven circulation system in the Atlantic Ocean [*Stommel*, 1957; *Gordon*, 1986]. It consists of four main branches. First, surface currents transport water from the Southern Atlantic across the equator and bring warm and saline water to the high latitudes of the North Atlantic. Second, surface water loses heat to the overlying cold atmosphere, densifies, loses buoyancy, and is, in so-called deep water formation regions of the North Atlantic, mixed with the underlying waters to up to a couple of kilometers depth through open ocean convection. Third, at depth, return currents

transport water southward across the equator and back into the South Atlantic. This deep southward flow is largely concentrated in the so-called Deep Western Boundary Current (DWBC). Fourth, these southward flowing waters are brought back up to the ocean surface via upwelling processes that take place over large areas of the Southern Ocean [*Talley*, 2013]. For a thorough description of the AMOC, the reader is referred to *Kuhlbrodt et al.* [2007, and references therein]. The four branches together form two overturning cells, an upper one with waters formed at high northern latitudes (North Atlantic Deep Water; NADW) and a lower one with waters formed by deep convection in the high latitudes of the Southern Ocean (Antarctic Bottom Water; AABW). A third major water mass that can be distinguished in the Atlantic and that is of importance in this manuscript is Antarctic Intermediate Water (AAIW), the shallowest of the three that is mostly formed due to intense wind-related mixing in the Southern Ocean.

Under present-day conditions, the formation of NADW mainly takes place at specific deep convection sites in the Nordic Seas and the Labrador Sea [*McCartney and Talley*, 1984; *Marshall and Schott*, 1999]. Changes in the temperature and salinity of the surface waters in these regions can cause significant changes in the volume of water that is able to sink into the deep ocean and alter the overall strength of the AMOC. By transporting large volumes of water, the AMOC transfers significant amounts of heat to the higher latitudes of the Northern Hemisphere (NH). Here this heat is released to the atmosphere, thereby acting as an important control on the climate of this region.

To reconstruct past variations in AMOC strength and deep-ocean water mass characteristics, several different methods are used to retrieve proxy-based information from marine sediment cores. For instance, the grain size characteristics of the sortable silt fraction are an indicator of the speed of local bottom currents [*McCave et al.*, 1995; *McCave and Hall*, 2006; *Thornalley et al.*, 2013a, 2013b], and the carbon isotopic composition (δ^{13}C) of benthic foraminifera provide information on the ventilation of deep-ocean water masses [*Shackleton*, 1977; *Duplessy et al.*, 1981]. The aforementioned methods reveal only limited aspects of the complex nature of the AMOC. Climate models are alternative and complementary tools that can be employed to investigate the evolution of the AMOC in its full complexity, notwithstanding limitations like the coarse spatial resolution (in this study 3° longitude by 3° latitude) and the limited representation of small-scale processes, such as mixing. Yet to evaluate simulated AMOC characteristics on timescales longer than covered by observational records, a comparison with paleoclimate reconstructions is imperative. A common approach is to compare the simulated maximum meridional overturning stream function in the North Atlantic (or the volume transport across a certain latitude) with reconstructions of changes in deep sea ventilation (δ^{13}C) or bottom water flow speeds (sortable silt; SS). In both of these cases the model-data comparison is indirect since local δ^{13}C and flow speed signals possibly have a complex and nonlinear relationship to changes in the overall strength of the AMOC. A more direct model-data comparison has been achieved in a number of studies through forward modeling of δ^{13}C [*Brovkin et al.*, 2007; *Bouttes et al.*, 2009, 2010, 2011]. However, these simulations were performed with two-dimensional ocean models and only focused on a single water mass property, while, as was pointed out by *Praetorius et al.* [2008], the complex spatial and temporal nature of the AMOC requires information from both water mass and dynamical proxies. To this end we will use a three-dimensional global climate model of intermediate complexity that includes full carbon cycle dynamics and a prescribed evolution of the AMOC to enable a direct model-data comparison of deep-ocean changes in flow speeds and δ^{13}C.

In this manuscript we focus on the AMOC evolution during the Last Interglacial period (LIG; ~129–116 ka; [*Shackleton et al.*, 2003]; ka indicates kiloyears before present) as a test case of the applicability of our model-based methodology that combines flow speeds and δ^{13}C to constrain changes in deep-ocean circulation. The LIG is a highly interesting period to test the ability of climate models to simulate changes in deep-ocean circulation within a relatively warm, interglacial climate. First, the thermal maximum of the LIG was probably warmer than present day [e.g., *CAPE Members*, 2006; *Wanner et al.*, 2008; *Turney and Jones*, 2010; *McKay et al.*, 2011; *Sánchez Goñi et al.*, 2012], leading to smaller Greenland and Antarctic ice sheets and a higher global sea level than today [*Koerner*, 1989; *Tarasov and Peltier*, 2003; *de Vernal and Hillaire-Marcel*, 2008; *Kopp et al.*, 2009; *Dutton and Lambeck*, 2012; *NEEM community members*, 2013]. The contribution of the Greenland ice sheet (GIS) to the sea level high stand is estimated to be 0.6 to 5.5 m sea level equivalent [*Alley et al.*, 2010; *Stone et al.*, 2013]. Second, the LIG and the preceding deglaciation are periods of AMOC reorganizations, as indicated by a large number of proxy-based reconstructions. During the penultimate deglaciation (roughly until 130 ka), the formation of NADW was very limited

[*Oppo et al.*, 1997]. No consensus on the evolution of the AMOC through the LIG has been reached to date [*Hillaire-Marcel et al.*, 2001; *Hodell et al.*, 2009; *Sánchez Goñi et al.*, 2012; *Govin et al.*, 2012]. However, it appears that it was only during the later part of the LIG (after ~126 ka) that the characteristics of the AMOC became similar to the present-day, full-strength state [*Hodell et al.*, 2009; *Sánchez Goñi et al.*, 2012; *Govin et al.*, 2012], while in the period in between (~130–126 ka) the AMOC characteristics and strength were weakened with respect to the present-day state. *Govin et al.* [2012] found proxy evidence that this weakened AMOC was likely caused by a "northerly" freshwater source. This is corroborated by a number of modeling studies where a weakened AMOC is simulated under the continued influence of enhanced ice sheet melting in the early LIG, for instance, enhanced GIS melt [*Otto-Bliesner et al.*, 2006; *Govin et al.*, 2012; *Bakker et al.*, 2012, 2013a; *Sánchez Goñi et al.*, 2012]. However, we note that a causal relationship between GIS melt and a weakened AMOC during the early LIG AMOC is not easily established. Moreover, *Bakker et al.* [2013a] have shown that the available GIS meltwater was probably insufficient to keep the AMOC significantly weaker for a prolonged period of time (3–5 ky).

Here we present the results of a 12 ky long transient climate simulation covering the LIG period from 132 to 120 ka. The simulation was performed with the Earth system model of intermediate complexity *i*LOVECLIM [*Roche*, 2013; *Bouttes et al.*, 2014] that includes a module for carbon isotope dynamics. To study changes in flow speeds and δ^{13}C in response to changes in the AMOC and enable a first model-data comparison, we introduce a meltwater flux that tunes the simulated AMOC to represent the general LIG AMOC evolution deduced from proxy-based reconstructions [*Hodell et al.*, 2009; *Sánchez Goñi et al.*, 2012; *Govin et al.*, 2012]. The results will be used to (i) investigate the factors controlling simulated changes in deep sea flow speeds and δ^{13}C throughout the forced LIG AMOC evolution, (ii) investigate the impact of these factors on different spatial scales, (iii) describe the impact of changes in the vertical water mass structure on simulated flow speed and δ^{13}C evolution, and (iv) use this knowledge in a test case model-data comparison of LIG AMOC evolution.

2. Methods and Model Evaluation

In this section we will first provide a description of the climate model and then provide an evaluation of the model output with modern observations of several variables that are key to the topic of this manuscript. In section 2.3 the LIG model scenario is presented, and finally a detailed description is given of the methodology to investigate the importance of different large-scale driving factors on the simulated evolution of flow speeds and δ^{13}C. Note that the data and methodology of the preliminary LIG model-data comparison are only presented in section 4.

2.1. Model Description

The *i*LOVECLIM Earth system model [*Roche*, 2013; *Bouttes et al.*, 2014] is a code fork of LOVECLIM version 1.2 [*Goosse et al.*, 2010]. *i*LOVECLIM includes a representation of the atmosphere, ocean, sea ice, and the land surface and its vegetation as in LOVECLIM version 1.2. The atmospheric component is ECBilt [*Opsteegh et al.*, 1998], an intermediate complexity spectral T21, three-level quasi-geostrophic model. The sea ice ocean component is CLIO3 [*Goosse and Fichefet*, 1999], a free-surface primitive equation model with a horizontal resolution of 3° longitude by 3° latitude and 20 vertical levels. The vegetation component is VECODE [*Brovkin et al.*, 2002], which simulates dynamical vegetation changes as a function of the climatic conditions.

Our *i*LOVECLIM version includes full carbon cycle dynamics throughout all components of the climate (see *Bouttes et al.* [2014] for a thorough description of the carbon cycle). The oceanic carbon cycle includes inorganic carbon, O_2, the nutrients phosphate and nitrate, and six organic tracers: phytoplankton, zooplankton, dissolved organic carbon, slow dissolved organic carbon, particulate organic carbon, and calcium carbonate. Phytoplankton synthesizes carbon in the first 100 m of the water column using light and nutrients. When it dies, it sinks and is partly grazed by zooplankton. Part of the plankton is remineralized following fixed remineralization profiles and exuded to both dissolved organic carbon and particulate organic carbon. The air-sea carbon flux is computed from the CO_2 partial pressure gradient. All carbon variables include ^{13}C isotopes and are advected and mixed via the *i*LOVECLIM advection-diffusion scheme. The terrestrial biosphere includes carbon in leaves, wood, litter, and soil. Photosynthesis depends on the local

precipitation, temperature, and the atmospheric CO_2 concentration. The calculated $\delta^{13}C$ ratio of the ^{13}C and ^{12}C isotopes is defined as

$$\delta^{13}C = 1000\left(\frac{R}{R_{\text{ref}}} - 1\right)$$

$$\text{with } R = \frac{13C}{12C}$$

R_{ref} is the Peedee belemnite carbon isotope standard that corresponds approximately to averaged limestone [*Craig*, 1957].

The $\delta^{13}C$ distribution in the ocean, atmosphere, and terrestrial biosphere depends on a number of processes. In the ocean, it depends on the air-sea exchange, transport, and fractionation through the marine biology. In the terrestrial biosphere, the $\delta^{13}C$ distribution only depends on the exchange with the atmosphere and biological fractionation. The atmospheric $\delta^{13}C$ distribution is a passive reservoir that is fully driven by changes in both the ocean and the terrestrial biosphere. Through preferential uptake of the lighter ^{12}C over ^{13}C during photosynthesis of both marine and terrestrial organisms, $\delta^{13}C$ values of the environment increase. Remineralization of ^{12}C-rich carbon in the ocean tends to decrease $\delta^{13}C$ values. A slightly modified exponential carbon remineralization profile [*Bouttes et al.*, 2014] is prescribed following *Brovkin et al.* [2002]. Note that when discussing oceanic $\delta^{13}C$ in the remainder of this manuscript, we refer to $\delta^{13}C$ of the inorganic carbon dissolved in seawater.

2.2. Evaluation of the Present-Day Atlantic Deep-Ocean Circulation in the *i*LOVECLIM Model

Bouttes et al. [2014] have previously shown that *i*LOVECLIM results compare favorably with observations of climatic variables such as temperature and salinity and the distributions of, for instance, nutrients, oxygen, carbon, and the carbon isotopes ^{13}C and ^{14}C. Moreover, a comparison with a range of state-of-the-art general circulation models has revealed that *i*LOVECLIM, despite its lower resolution and complexity, generally falls in the middle of the range covered by other models in terms of the horizontal and vertical distribution of different climatic variables and carbon cycle tracers [*Bouttes et al.*, 2014]. An important bias in the simulated $\delta^{13}C$ distribution is the too rapid $\delta^{13}C$ decrease of NADW along its southward path, possibly related to diffusion being too high [*Bouttes et al.*, 2014]. Since the present study focuses specifically on simulated vertical $\delta^{13}C$ profiles in the deep Atlantic, we performed an additional evaluation of the model results, under present-day boundary conditions, by comparison with observations from a number of observational transects in the Atlantic. In the following we compare modern observational data with a preindustrial climate simulation. We acknowledge that this is not a perfect comparison but assume that the changes in large-scale deep-ocean characteristics over the last centuries are sufficiently small [*Lund et al.*, 2006; *Jones et al.*, 2009].

For most regions, the vertical structure of absolute values of temperature, salinity, and $\delta^{13}C$ in the Atlantic Basin (see Figure 1 for exact locations), as simulated with the *i*LOVECLIM model for preindustrial conditions, compare well with the observations, but there are also a number of offsets (Figure 2; observational data from the National Oceanic and Atmospheric Administration (NOAA) World Ocean Database). The first apparent mismatches are the overly cold temperatures below ~2.5 km and the $\delta^{13}C$ values that are too low in the southeastern Atlantic and, to a lesser degree, in the equatorial (western) Atlantic, a model bias previously described by *Caley and Roche* [2013]. The biases in the deep ocean are also apparent in most other parts of the Atlantic and result from the overly vigorous formation of AABW that is too cold, in the Southern Ocean [*Bouttes et al.*, 2014]. Disagreement between observations and model results is also found in the Nordic Seas, where the inflow of warm and saline Atlantic waters to these high northern latitudes is too great, in agreement with the findings of *Bouttes et al.* [2014]. Connected to this bias is the offset of simulated $\delta^{13}C$ in the Norwegian Sea toward too high values. These could be the direct result of the too high inflow of Atlantic waters or a consequence of too large biological production related to the local temperature bias. Additional sensitivity experiments are required to separate both effects. Despite these model biases in temperature, salinity, and $\delta^{13}C$, the agreement in the overall structure and gradients gives confidence when using the model to study past changes in the deep-ocean circulation. Nonetheless, in a relatively simplified and low-resolution model like the one used here, important details such as the precise location and depths of the different water masses and currents should be treated with caution. There is thus a gap between the spatial
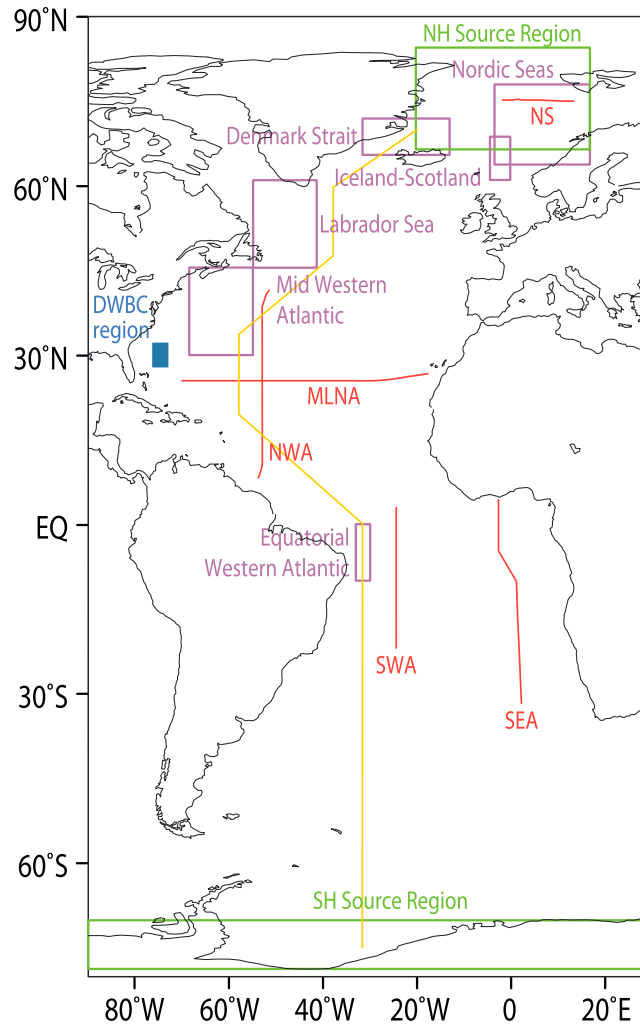
Figure 1. Geographical position of regions and transects specified throughout the manuscript. The five observational data transect depicted in Figure 2 are given in red with the corresponding abbreviations: southeastern Atlantic (SEA), southwestern Atlantic (SWA), midlatitude North Atlantic (MLNA), northwestern Atlantic (NWA), and Norwegian Sea (NS). The geographical bounds over which averaged ocean surface source region $\delta^{13}C$ are computed are given in green. The meridional western boundary transect shown in Figure 7 is given in yellow. The regions specified in Figure 10 are given in purple. The blue area shows the DWBC region from which simulated and reconstructed data are compared in Figures 11–13.

scales considered by the climate model and by proxy-based reconstructions. However, it is important to realize that when using a climate model to study the long-term evolution of the climate system, a compromise has to be made in terms of the spatial resolution of the model. With the currently available computing power multimillennial climate simulations cannot be performed with much higher resolution than that presented here.

2.3. LIG Scenario Description

We have performed a 12 ky long transient simulation of the LIG climate from 132 to 120 ka. The simulation is forced with changes in top-of-the-atmosphere insolation caused by changes in orbital parameters [*Berger*, 1978] and by changes in greenhouse gas concentrations derived from ice core measurements (*Luthi et al.* [2008], *Loulergue et al.* [2008], and *Schilt et al.* [2010] for CO_2, CH_4, and N_2O, respectively; forcings in line with the PMIP3 protocol; Figure 3). Note that CO_2 is an intrinsic model variable in terms of carbon dynamics, but this variable is decoupled from the CO_2 concentrations that are used as radiative forcing. Previous studies have shown that equilibrium and transient simulations of the LIG climate with the *i*LOVECLIM model compare reasonably well with surface climate reconstructions and fall within the range of results from general circulation models [*Bakker et al.*, 2013b; *Lunt et al.*, 2013].

Proxy-based reconstructions broadly agree on the evolution of the AMOC's strength throughout the LIG period and the preceding deglaciation: a weak to nearly collapsed AMOC during the final part of penultimate deglaciation (~132–130 ka), a weakened AMOC during the early LIG (~130–126 ka), and a full-strength AMOC after ~126 ka that closely resembles the present-day situation [*Hodell et al.*, 2009; *Sánchez Goñi et al.*, 2012; *Govin et al.*, 2012]. To tune the simulated AMOC qualitatively to the evolution outlined above, we impose a freshwater forcing that is designed based on findings from a large number of LOVECLIM sensitivity experiments performed by *Bakker et al.* [2012]. We start the simulation at 132 ka with a freshwater flux of ~0.187 sverdrup (Sv = 10^6 m^3 s^{-1}) that is distributed equally around Greenland, and thereafter the freshwater flux decreases linearly toward zero at ~123.5 ka (Figure 3). Initial conditions for the transient simulation are derived from a 1 ky long equilibrium experiment including 132 ka insolation, greenhouse gas concentrations, and a ~0.187 Sv freshwater flux. The climate is in quasi-equilibrium after 1 ky with a mean ocean temperature change of only −0.0047°C over the last 100 years comparable to the natural variability in the system
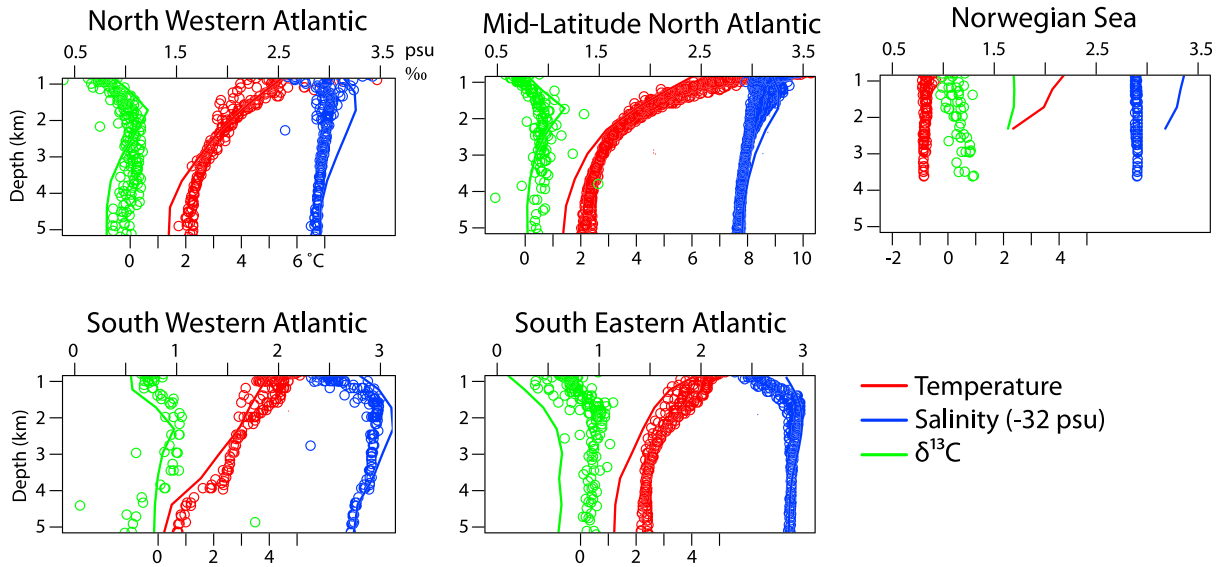
Figure 2. Comparison of single grid cell 100 year mean *i*LOVECLIM model outputs under preindustrial boundary conditions (closed diamonds) with observational data (open circles) available for five transects from the NOAA World Ocean Database 2009 [*Boyer et al.*, 2009] using vertical profiles of both temperature (°C), salinity (psu; constant 32 psu is subtracted), and δ^{13}C (‰). We have limited the length of the different observational transects in order to obtain overall coherent vertical profiles. See Figure 1 for geographical positions of the transects.

($1\sigma = 0.0045$°C for yearly averaged mean ocean temperature changes in a control simulation). We acknowledge that the initial conditions of the experiment, e.g., the characteristics of the different water masses and carbon reservoirs, are poorly constrained. However, we would argue that the possible impacts are mostly limited to the first 1–2 ky of the simulation; after that the uncertainties in the initial conditions become of less importance [*Renssen et al.*, 2006]. Apart from changes in insolation, greenhouse gas concentrations, and freshwater flux, all boundary conditions are kept at present-day values.
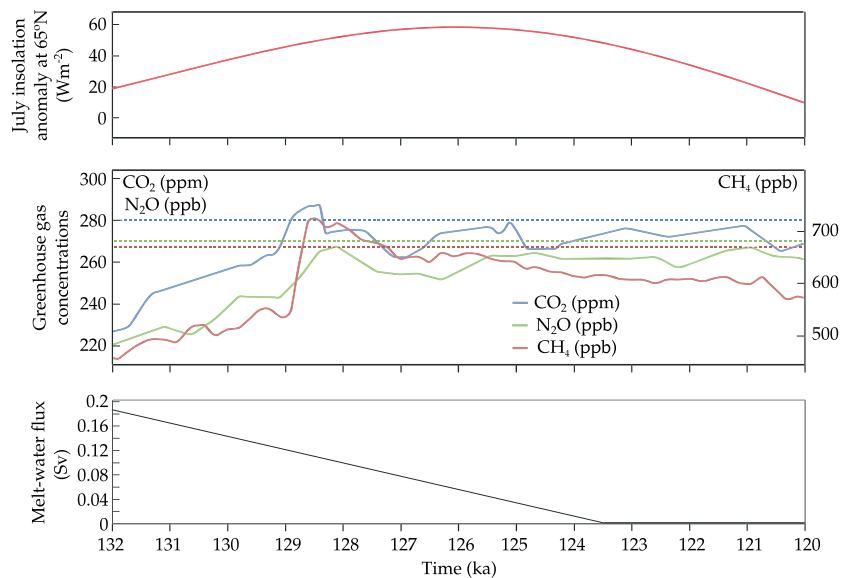

Figure 3. Experimental setup. (top) July insolation anomalies (W m^{-2}; compared to modern-day values) at 65°N [*Berger*, 1978]. (middle) Reconstructed evolution of the main greenhouse gas concentrations (*Luthi et al.* [2008], *Loulergue et al.* [2008], and *Schilt et al.* [2010] for CO$_2$, CH$_4$, and N$_2$O, respectively). The changes in insolation and greenhouse gas concentrations imposed on the LIG climate simulation are in accordance with the PMIP3 protocol (http://pmip3.lsce.ipsl.fr/). (bottom) The imposed freshwater forcing (Sv) in the LIG climate simulation. It is designed after the findings of *Bakker et al.* [2012] in order to yield an AMOC evolution in line with proxy-based finding [*Hodell et al.*, 2009; *Sânchez Goñi et al.*, 2012; *Govin et al.*, 2012].

By tuning the simulated AMOC evolution, we circumvent the common difficulties of other so-called hosing experiments of having to pinpoint the source(s) and amount of the freshwater input into the ocean during the final stage of the penultimate deglaciation and the LIG. Moreover, through this method, we deal with the strongly model-dependent sensitivity of the AMOC to perturbations of the freshwater budget of the North Atlantic. However, we emphasize that the applied GIS freshwater forcing per se is purely hypothetical in terms of its temporal evolution, spatial distribution, and magnitude and solely serves to tune the AMOC evolution. Nonetheless, a sizable freshwater flux of northern origin during the period covered by the first half of the simulation is not necessarily unrealistic, since this period includes both changes in the volume of the GIS and deglacial meltwater fluxes from remaining continental ice sheets covering North America and Eurasia [*Svendsen et al.*, 2004; *Nicholl et al.*, 2012]. Nonetheless, the constructed scenario and resulting AMOC evolution are uncertain, an issue that we will revisit in section 4 when comparing simulated and reconstructed flow speed and δ^{13}C values.

As a consequence of the applied freshwater forcing, the simulated LIG climate is characterized by a distinct evolution of the AMOC strength. During the first 1–2 ky of the studied interval, the AMOC strength is close to 6 Sv (Figure 4a), which in this particular model resembles a situation without large-scale deep convection in the North Atlantic. During the period ~131–126 ka the AMOC strengthens toward a value of ~14 Sv, and afterward a rapid increase is simulated until ~123.5 ka up to a present-day-like AMOC strength of ~23 Sv. Simulated changes in the convective layer depth (a measure of local convective activity; not shown here) reveal that the ~130–126 ka AMOC increase is largely caused by initiation and invigoration of deep water formation in the Nordic Seas. Deep convection in the Labrador Sea only starts after ~125–124 ka and continues to increase until the end of the simulation at 120 ka. North Atlantic surface and deep-ocean climate characteristics for similar LIG AMOC configurations have previously been described for LIG LOVECLIM simulations by *Bakker et al.* [2012, 2013a, 2013b].

2.4. Simulated Factors Affecting Flow Speeds and δ^{13}C

To investigate the main factors that drive the simulated changes in flow speeds and δ^{13}C, we propose to mimic the simulated evolution of the two variables by a linear combination of the evolution of a number of driving factors. We first outline here the main driving factors and then present the linear model used. Note that in the remainder of the text we will use the term "driving factors" to refer to factors that are thought to have an important impact on the millennial-scale evolution of variables under consideration in this study.

The evolution of deep-ocean current flow speeds in the Atlantic is closely related to changes in the volume transport in the upper and lower circulation cells of the AMOC, (i) volume transport of northern sourced deep water (NSDW; Figure 4a) and (ii) volume transport of southern sourced deep water (SSDW; Figure 4b). Next to these large-scale (>10.000 km) driving factors, local flow pattern changes can also strongly impact the simulated evolution of flow speeds, caused by shifts in the position or strength of local return currents (typical scale of ~100 km) or gyre circulation (typical scale of ~1000–5000 km). A complicating factor in the interpretation of flow speed changes is caused by the possibility that the upper and lower circulation cells of the AMOC can deepen or shoal, with important consequences for the depths where the different water masses are present. To investigate the causes of simulated changes in deep flow speeds, we calculate the least squares residuals fit between the simulated flow speed time series in a particular grid cell and a linear combination of the normalized time series of the driving factors, the strength of NSDW and SSDW, respectively.

The evolution of the local flow speed (q) with time (t) is a function of the local horizontal velocity evolution vector $v(t)$ following

$$q(t) = \|\bar{v}(t)\| = \sqrt{\bar{v}_x^2 + \bar{v}_y^2}$$

where the overbar denotes a 100 year average, the double vertical lines the norm of vector $v(t)$, and the subscripts x and y the velocity components in the zonal and meridional directions, respectively. Note that we assume vertical velocities to be sufficiently small compared to horizontal velocities to be neglected. The different driving factors (F_n) as a function of time are normalized following

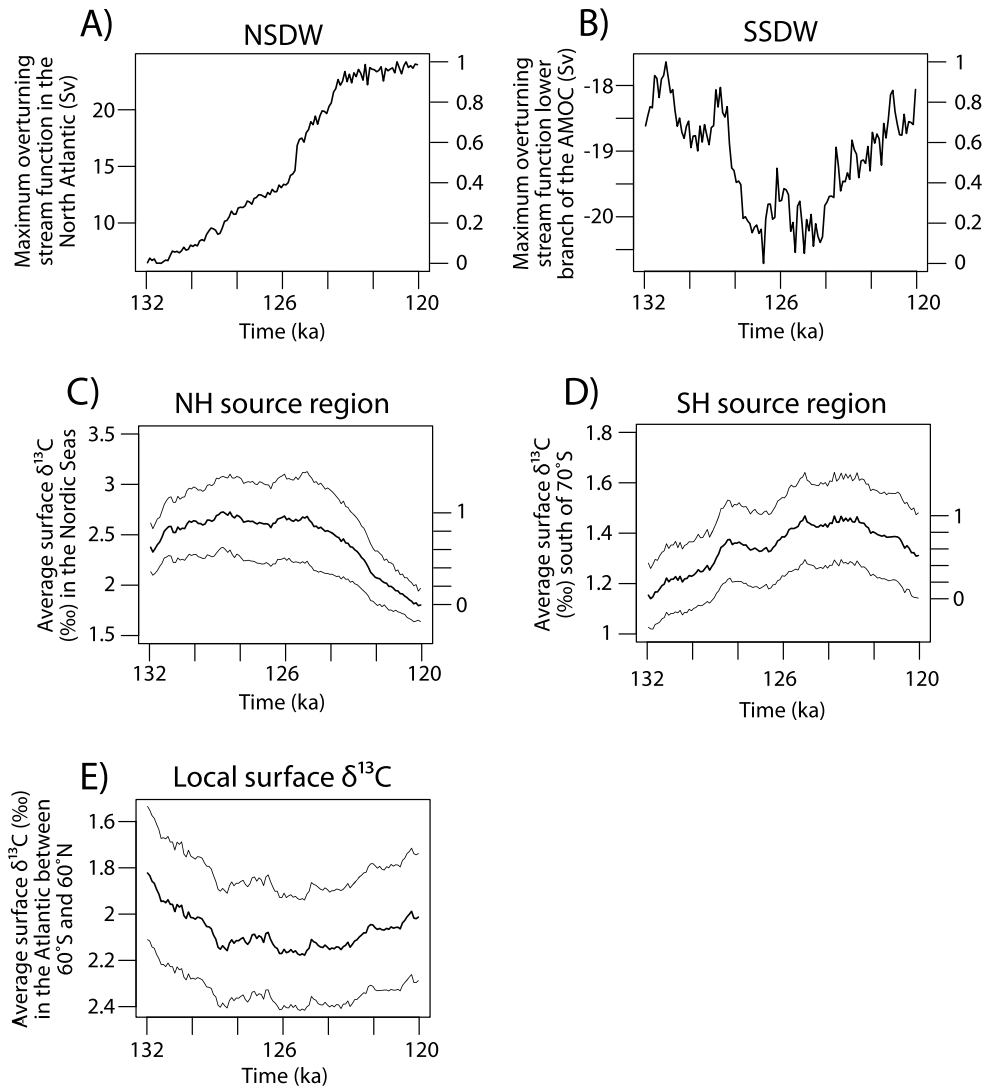$$F_n(t) = \frac{F(t) - F_{\min}}{F_{\max} - F_{\min}}$$

Figure 4. Simulated drivers of the evolution of flow speeds and $\delta^{13}C$ for 132–120 ka: (a) transport (Sv) of northern sourced deep waters (NSDW) taken here as the maximum overturning stream function in the upper cell of the AMOC; (b) transport (Sv) of southern sourced deep waters (SSDW) taken here as the maximum overturning stream function in the lower cell of the AMOC; (c) mean surface $\delta^{13}C$ in the main Northern Hemisphere source region (‰); (d) mean surface $\delta^{13}C$ in the main Southern Hemisphere source region (‰; see Figure 1 for spatial extent of regions); (e) local surface $\delta^{13}C$ (‰; note the reversed vertical axis). Note that to calculate the importance of remineralization, local (single grid cell) surface $\delta^{13}C$ values are used. It is only to provide an indication of the general surface $\delta^{13}C$ evolution that we give here the average surface signal over the whole Atlantic basin (60°S–60°N by 70°W–20°E). In Figures 4c–4e, gray lines indicate the variability ($\pm 1\sigma$) within the region of interest. For the drivers we also show corresponding normalized values (secondary y axis) that are used in the linear correlation model (except for the local surface $\delta^{13}C$ evolution that are shown for reference only). All values shown and used for calculations are 100 year averages.

We assume a linear relationship between the local flow speed evolution $q(t)$ and the two normalized driving factors that follow from the time series of NSDW ($F_{nw}(t)$) and SSDW ($F_{sw}(t)$):

$$q(t) = a_{nw}F_{nw}(t) + a_{sw}F_{sw}(t)$$

in which the parameters a_{nw} and a_{sw} are found by minimizing the sum of

$$S(a_{nw}, a_{sw}) = \sum_{t=1}^{n}(q(t) - a_{nw}F_{nw}(t))^2 + \sum_{t=1}^{n}(q(t) - a_{sw}F_{sw}(t))^2$$

Through this methodology we make two important assumptions, first that the importance of the two driving factors at a single location do not change in time and second that the two driving factors are independent (see section 4.1 for further discussion).

Similarly, we investigated the main factors affecting the simulated changes in local $\delta^{13}C$. As for flow speed, two important factors are volume transport of (i) NSDW and (ii) SSDW (Figures 4a and 4b). However, in the case of $\delta^{13}C$, it is not only the transported volumes of deep water that are important but also the $\delta^{13}C$ surface values in the regions where the deep waters are formed, i.e., (iii) the NH source region (Figure 4c), and (iv) the Southern Hemisphere (SH) source region (Figure 4d). For the evolution of NH source waters, an average is taken over the surface water between 68°N–86°N and 20°W–17°E (Figure 1). Similarly, we obtained the SH source water signal from an averaged $\delta^{13}C$ surface signal over all grid cells south of 70°S (Figure 1). The final factor impacting the $\delta^{13}C$ evolution is (v) changes in remineralization of organic matter that are in turn closely linked to changes in local surface productivity and therewith the local surface $\delta^{13}C$ evolution (Figure 4e). The local surface $\delta^{13}C$ evolution is calculated as the simulated $\delta^{13}C$ time series from the surface ocean grid cell at that specific location. Note that the mean surface $\delta^{13}C$ evolution shown in Figure 4e is strongly related to the LIG evolution of continental vegetation simulated by the *i*LOVECLIM model (not shown). In comparison to the evolution of flow speeds, the latter three factors greatly increase the complexity of explaining the evolution of $\delta^{13}C$.

To establish the importance of these different factors for the local $\delta^{13}C$ evolution, we combine the resulting normalized time series in a linear model and calculate the least squares residuals fit between this model and the $\delta^{13}C$ time series, in a way similar to the method applied for local flow speeds. An important note to make is that we assume all correlation factors to be positive except for a negative correlation between $\delta^{13}C$ and SSDW and a negative correlation between $\delta^{13}C$ and local surface $\delta^{13}C$ values. Indeed, the SH source region is a source of low $\delta^{13}C$ values and an increase in the export of SSDW (characterized by low $\delta^{13}C$ values) lowers local $\delta^{13}C$ values. In addition, the negative correlation between the evolution of $\delta^{13}C$ and local surface $\delta^{13}C$ values stems from the fact that an increase in surface biological productivity increases the surface $\delta^{13}C$, while its subsequent remineralization in the deeper ocean decreases $\delta^{13}C$ at depth [*Kroopnick*, 1985]. We acknowledge that the resulting NH and SH source region signals and the local surface $\delta^{13}C$ signal are simplifications, but we find that their overall temporal evolution appears to be robust (Figures 4c–4e). It is this temporal evolution and not the absolute values or amplitude of the changes that impact the calculated correlation factors since all values involved in these calculations are normalized. The linear model for $\delta^{13}C$ reads

$$\delta^{13}C(t) = b_{nw}F_{nw}(t) - b_{sw}F_{sw}(t) + b_{ns}F_{ns}(t) + b_{ss}F_{ss}(t) - b_lF_l(t)$$

with the subscripts standing for NH source waters (ns), SH source waters (ss), and local surface $\delta^{13}C$ (l). As for flow speeds, the values of the parameters b_x are found by minimizing the sum of

$$S(b_{nw}, b_{sw}, b_{ns}, b_{ss}, b_l) = \sum_{t=1}^{n} \left(\delta^{13}C(t) - b_{nw}F_{nw}(t)\right)^2$$
$$-\sum_{t=1}^{n} \left(\delta^{13}C(t) - b_{sw}F_{sw}(t)\right)^2 + \sum_{t=1}^{n} \left(\delta^{13}C(t) - b_{ns}F_{ns}(t)\right)^2$$
$$+\sum_{t=1}^{n} \left(\delta^{13}C(t) - b_{ss}F_{ss}(t)\right)^2 - \sum_{t=1}^{n} \left(\delta^{13}C(t) - b_lF_l(t)\right)^2$$

It is important to stress that the linear model used for correlation calculations between the different factors and the simulated flow speed and $\delta^{13}C$ signals is based on single grid cell time series. Thus, no spatial information about the water mass structure or pathways of the deep ocean is embedded in the linear correlation model. A priori, the focus on large-scale driving factors of flow speeds and $\delta^{13}C$ and neglect of small-scale forcings does not allow an investigation of regional or single grid cell results. However, we argue that the emergence in specific regions of coherent spatial patterns that resemble well-known water mass structures or pathways of the deep ocean reveals the strong link with large-scale driving factors in those regions and therewith provides confidence in the investigation of the results on regional and single grid cell scales. For the same reason, no statistical significance levels of the correlations are computed,
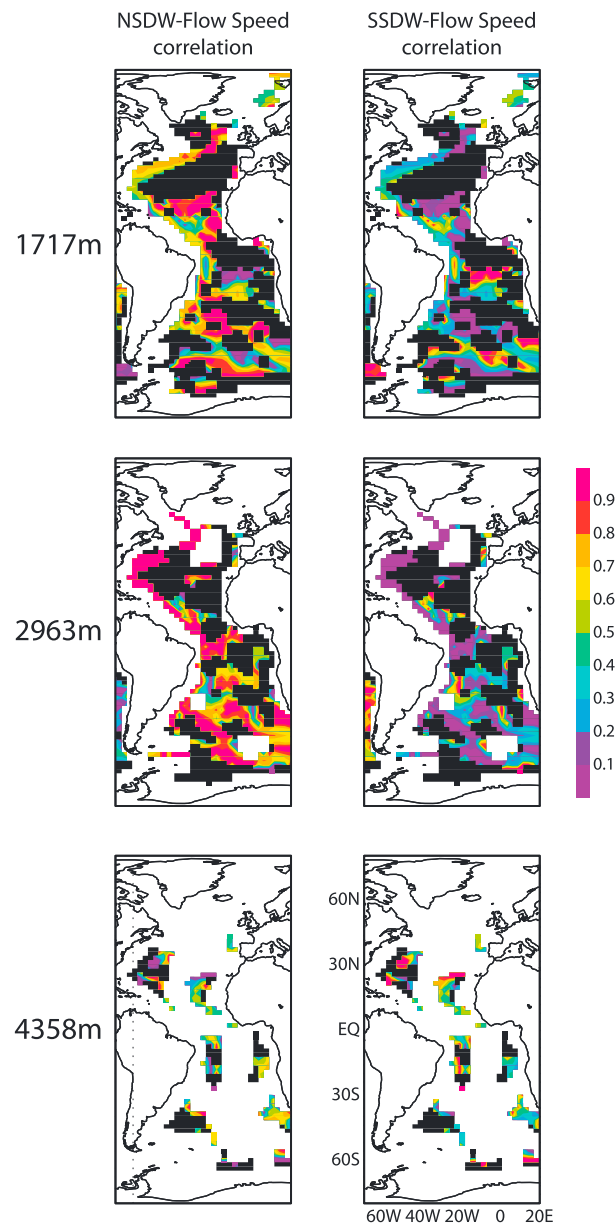
Figure 5. (top to bottom) For three different depth levels, the correlation coefficients in the Atlantic basin are shown between the simulated 132–120 ka evolution of (left column) flow speeds and NSDW transport and (right column) flow speeds and SSDW transport. The correlations are based on a linear least squares model, and they are scaled per grid cell to ensure that the two correlation coefficients add up to 1. The grid cell is masked out (black) if the correlation between the flow speed evolution and the fit resulting from the linear model (i.e., a combination of both driving factors) is below 0.5. Note that the apparent limited area extent in this figure compared to Figure 6 stems from the fact that flow is calculated from density gradients for which a neighboring cell is required.

because it is the spatial coherency that at the end determines the credibility of the results. In line with this reasoning we first present the results for the largest, basin-wide scale and only zoom in on the smaller scales in particular regions for which spatially coherent correlations with the predetermined large-scale driving factors have been shown. Finally, it is important to note that a good correlation does not necessarily imply causality, and we will see in section 3 that critical evaluation of the model results is required to distinguish between the actual signal and the artifacts of the applied linear correlation model.

3. Results: Simulated Changes in Flow Speeds and $\delta^{13}C$

In the first part of section 3 we focus on the basin-scale correlation of the evolution of flow speed and $\delta^{13}C$ with the driving factors described in section 2.4. These results will then be compared with the overall proxy-based $\delta^{13}C$ signal that is found in a compilation of LIG $\delta^{13}C$ records from the Atlantic. This will provide a first-order test of the validity of the applied AMOC evolution. Afterward we will zoom in from the basin scale, via regional averages, to the grid cell scale evolution of flow speeds and $\delta^{13}C$, focusing on those regions for which we find spatially coherent correlations between the flow speed and $\delta^{13}C$ evolution and large-scale driving factors. The investigation of grid cell scale changes serves as the starting point of a local model-data comparison for the DWBC presented in section 4. It is through a local model-data comparison for a critical region like the DWBC that the validity of the methodology can potentially really be assessed and the realism of the applied AMOC evolution evaluated.

3.1. Basin Scale

The results of the correlation between the linear model of the two factors—NSDW and SSDW—and the simulated time series of local flow speeds reveal an overall scattered pattern with large differences over small spatial scales and many regions where the linear model cannot explain the evolution of local flow speeds (correlation <0.5; Figure 5). A pattern does emerge for the correlation with NSDW at the 2963 m model level and can be linked to the export of NADW from the overflow regions and along the western boundary of the Atlantic Basin.
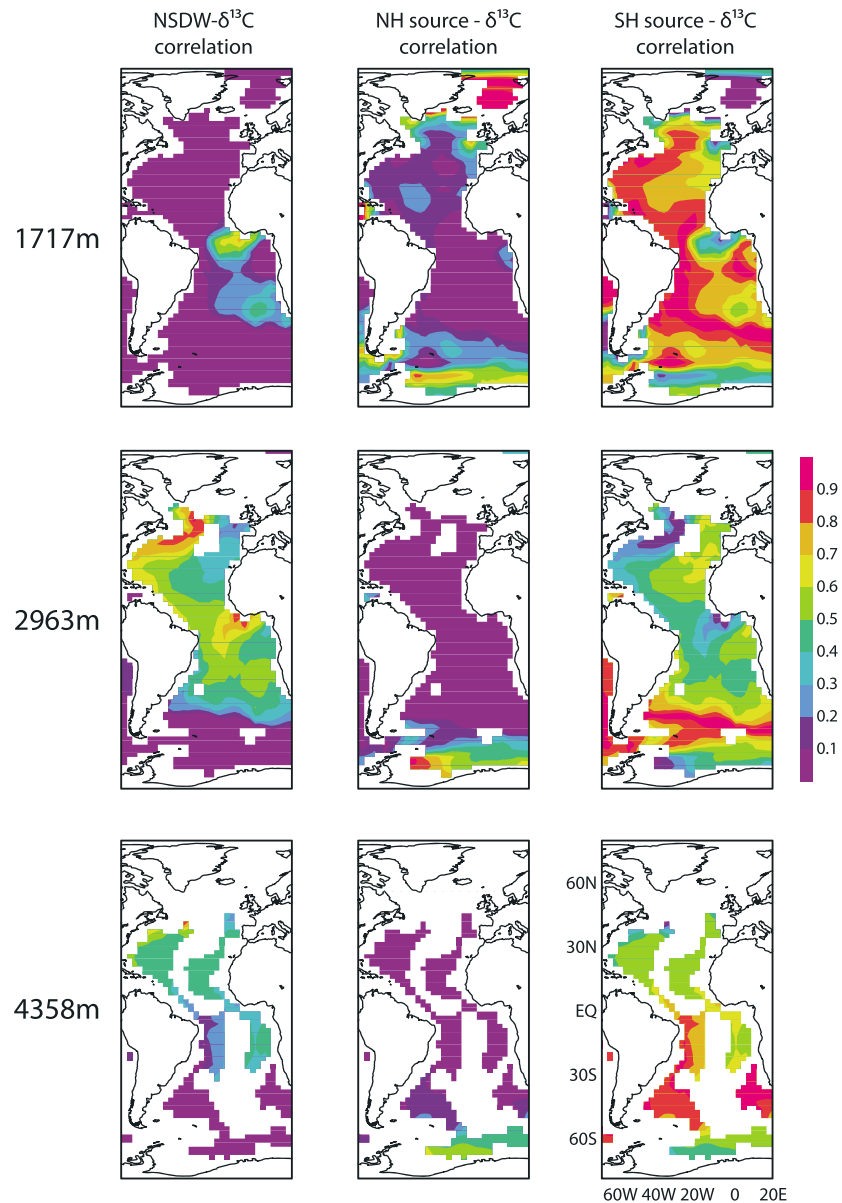
Figure 6. (top to bottom) For three different depth levels (top to bottom) the correlation coefficients in the Atlantic basin are shown between the simulated 132–120 ka evolution of (left column) δ^{13}C and NSDW transport, (middle column) δ^{13}C and NH source region δ^{13}C signal, and (right column) δ^{13}C and SH source region δ^{13}C signal. The correlations are based on a linear least squares model that includes, next to the three drivers listed here, also SSDW transport and the local surface δ^{13}C signal. The correlation coefficients are scaled per grid cell to ensure that the five correlation coefficients add up to 1. The correlations between SSDW transport and δ^{13}C and between the local surface δ^{13}C signal and δ^{13}C are not shown because they are nowhere above 0.2.

A correlation between the export of SSDW and the local flow speeds at the 4358 m level cannot be discerned in any part of the Atlantic, despite the fact that these abyssal regions of especially the South Atlantic are known to lie in AABW. Possibly, the lack of spatial coherency on the 4358 m level also relates to the limited horizontal extent of this depth level.

The correlations between local δ^{13}C and the different factors—NSDW, SSDW, NH source region, SH source region, and the δ^{13}C surface signal—offer much more spatially coherent patterns (Figure 6) and show that the linear model can explain most of the changes in local δ^{13}C (correlation >0.5). Note that according to our results, changes in SSDW and local surface δ^{13}C values have very little (<0.2) correlation with the δ^{13}C
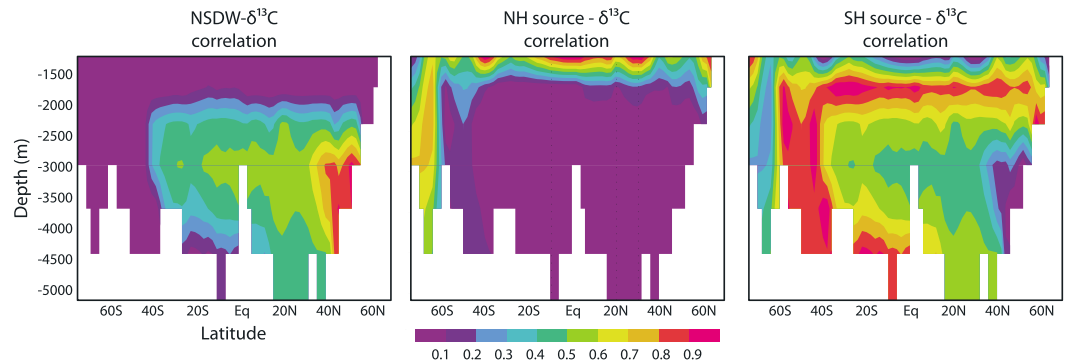
Figure 7. Meridional-depth cross section of correlation between NSDW, NH source, SH source, and $\delta^{13}C$. The cross section follows roughly the western boundary of the Atlantic basin (see Figure 1 for exact path) and is based on single grid cell values. See caption of Figure 6 for more information.

time series and are therefore neglected in the remaining analysis. Changes in SH source region $\delta^{13}C$ values dominate the correlation with the $\delta^{13}C$ evolution at the 1717 m model level. It is only in the Nordic Seas and along the northern limits of the North Atlantic that NH source region $\delta^{13}C$ changes are important. The apparent impact of NH source region $\delta^{13}C$ changes on Southern Ocean waters is addressed in section 4.2. The impact of the evolution of NSDW is very limited at 1717 m in the model. At the 2963 m level, the impact of NSDW dominates the correlation and reveals a decreasing pattern toward the south and higher correlation values along the western boundary of the Atlantic basin. SH source region $\delta^{13}C$ changes also explain an important part of the $\delta^{13}C$ signals at this depth, especially in the SH midlatitudes and the eastern part of the North Atlantic. At the 4385 m level, this trend continues with the importance of NSDW decreasing even further and the opposite trend for SSDW, overall explaining most of the evolution of $\delta^{13}C$.

To better connect the presented correlations to the different water masses of the deep Atlantic, a meridional-depth cross section (along the western boundary of the Atlantic; see Figure 1) and a zonal-depth cross section (average over 20°N–40°N) are made (Figures 7 and 8). The cross sections reveal a maximum correlation between the $\delta^{13}C$ evolutions and NSDW around 3000 m depth that deteriorates south of ~30° (Figure 7) and from the western boundary toward the eastern side of the Atlantic (Figure 8). This spatial pattern strongly suggests that these regions are bathed by NADW. SH source region $\delta^{13}C$ changes explain most of the $\delta^{13}C$ evolution in several regions: over all depth levels between 40°S and 60°S, below ~3500 m along the meridional transect, between 1500 and 2000 m from 40°S up until 50°N, and finally a general trend with decreasing importance of SH source region $\delta^{13}C$ changes going from the eastern side of the Atlantic toward the western side. These spatial patterns indicate a connection between the influence of SH source region $\delta^{13}C$ changes and the $\delta^{13}C$ evolution in the two most important southern sourced water masses: AAIW and AABW.
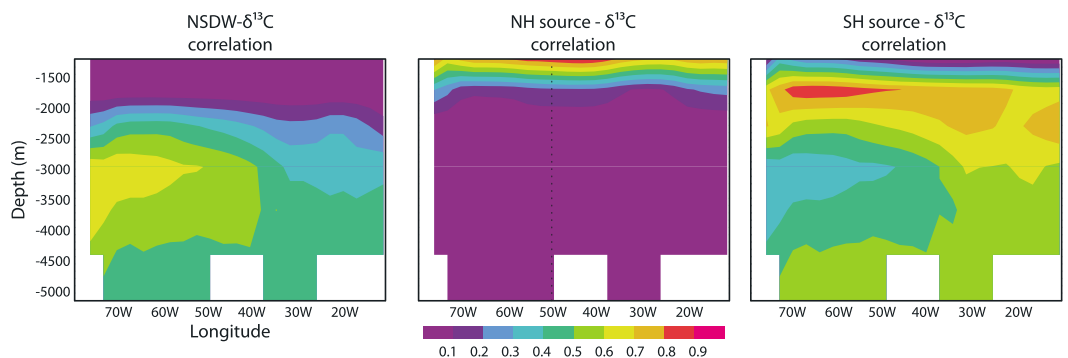

Figure 8. Zonal-depth cross section of correlation between NSDW, NH source, SH source, and $\delta^{13}C$ for the Atlantic basin, averaged between 20°N and 40°N. See caption of Figure 6 for more information.
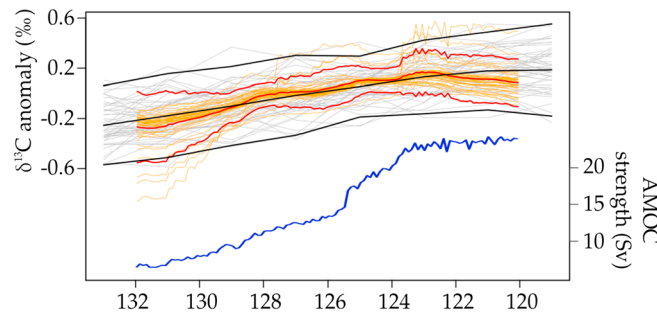
Figure 9. Atlantic basin-wide comparison of reconstructed and simulated $\delta^{13}C$ evolution. Mean reconstructed $\delta^{13}C$ anomalies (‰; middle black line) and variability (2σ; outer black lines). Averages and variability are based on 52 individual reconstructed $\delta^{13}C$ time series from the Atlantic basin (thin gray lines), that is, a subset of the *Oliver et al.* [2010] data set. Also given are the simulated mean (middle red line) and variability (2σ; outer red lines) averaged over the 52 grid cells that are closest to the core locations of the reconstructed $\delta^{13}C$ time series. The 52 individual simulated $\delta^{13}C$ time series are given by the thin orange lines. Anomalies were calculated with respect to site individual 133–119 ka or 132–120 ka means for the reconstructions and simulations, respectively. The correlation between the reconstructed and simulated mean time series is 0.96. For comparison the simulated evolution of the AMOC strength (the maximum overturning stream function in the North Atlantic) is given in blue.

We find high correlations between NH source region changes and the $\delta^{13}C$ evolution in most of the SH high latitudes as well as in waters above 1500 m (Figures 7 and 8). A physically sound mechanism that could transport this NH source region signal from the Nordic Seas to the SH high latitudes and into waters shallower than <1500 m is currently lacking, especially since its impact is absent from the main northern sourced water mass, NADW. This issue is discussed further in section 4.

3.2. Basin-Scale Model-Data Comparison of $\delta^{13}C$ Evolution

The signature of the AMOC evolution in the simulated $\delta^{13}C$ evolution observed on the basin scale allows for a first model-data comparison to provide credibility to the presented simulations and the forced LIG AMOC evolution. We compare a subset of the proxy-based $\delta^{13}C$ compilation of *Oliver et al.* [2010] to the simulated $\delta^{13}C$ evolution at the nearest model grid cell in both the horizontal and vertical. We use a total of 52 records from the *Oliver et al.* [2010] compilation, namely, all records that cover the simulated LIG period, 132–120 ka, and stem from the Atlantic region. These $\delta^{13}C$ records cover most of the Atlantic between ~50°S and 60°N and include different benthic foraminefera species (*Cibicidoides wuellerstorfi*, other *Cibicidoides* species, and *Uvigerina* species only). *Cibicidoides* species are assumed to record the $\delta^{13}C$ of inorganic carbon dissolved in ambient seawater, while *Oliver et al.* [2010] applied a correction of +0.85 ± 0.48‰ to $\delta^{13}C$ values measured on *Uvigerina* species. For a more thorough description of the $\delta^{13}C$ compilation we refer to *Oliver et al.* [2010]. This model-data comparison on the basin scale shows good agreement in the overall shape of the $\delta^{13}C$ evolution, the magnitude, and the spatial variability (Figure 9). This good correspondence on the basin scale provides confidence in the applied methodology and the idealized freshwater forcing applied in this study. Moreover, this result shows that an AMOC evolution similar to the one simulated by the model is a possible mechanism to explain the reconstructed basin-scale $\delta^{13}C$ changes. Nonetheless, it cannot be ruled out that a good agreement between the large-scale simulated and reconstructed $\delta^{13}C$ evolution is obtained for the wrong reasons. There are for instance indications from paleoclimate reconstructions that the gradual LIG increase in $\delta^{13}C$ was the result of changes in preformed $\delta^{13}C$ of NADW rather than an increase in the strength of the AMOC [e.g., *Fronval et al.*, 1998; *Bauch*, 2013]. In the next sections we will see that indeed in certain regions the $\delta^{13}C$ evolution is driven by changes in preformed $\delta^{13}C$ rather than the AMOC evolution. Potentially, a model-data comparison including both flow speeds and $\delta^{13}C$ for a region that shows large sensitivity to AMOC changes can help to distinguish the different potential factors driving such $\delta^{13}C$ evolution. Such a model-data comparison will be attempted in section 4.

3.3. Regional Scale

We have shown that on the large spatial scale of water masses and ocean basins, the simulated evolution of $\delta^{13}C$ is correlated to specific large-scale driving factors, whereas large-scale driving factors control the simulated flow speeds in specific regions only (section 3.1). To investigate how these relationships translate to the regional scale, we zoom in on several regions along the path of NADW and its formation regions (Figure 10) for which we found spatially coherent patterns in the correlation with large-scale driving factors: the Nordic Seas and its overflow points, the Labrador Sea region, and finally two locations along the DWBC close to the North American coast and the equatorial Brazilian coast (see Figure 1 for specific geographical positions). The evolution of flow speed and $\delta^{13}C$ for different regions and depth levels shown in Figure 10 results from
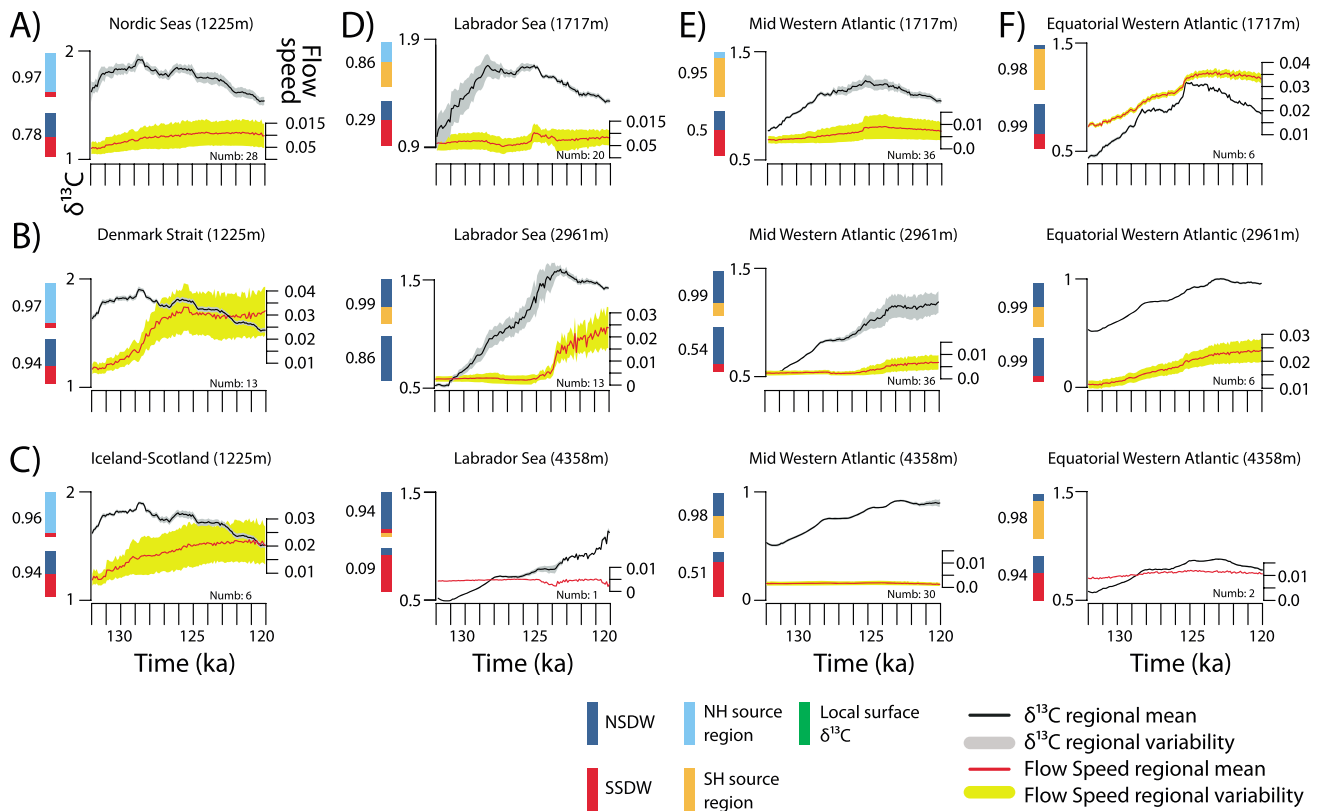
Figure 10. Simulated evolution of δ^{13}C (‰; black) and flow speed (m s^{-1}; red) for six key Atlantic regions for the period 132–120 ka. (a–c) The 1225 m level of, respectively, the Nordic Seas, Denmark Strait, and the Iceland-Scotland Ridge. The remaining columns give results for three different depth levels (1717, 2961 and 3662 m) for (d) the Labrador Sea, (e) the midwestern Atlantic, and (f) the equatorial Atlantic (see Figure 1 for geographical extent of the different regions). The gray and yellow bands give the variability (1σ) around the mean calculated on the individual grid cells within one key region (number of cells is given in right corner of individual plots). The vertical colored bars in front of the figures shown for every individual region and depth level indicate the relative importance of the different forcing mechanisms in the calculated best linear fit between the simulated δ^{13}C evolution and the drivers (upper color bar) and the flow speed evolution and the drivers (lower color bar; note that for flow speed only NSDW and SSDW are taken into account in the linear correlation model). The resulting best correlation is given in front of the color bars.

combining single grid cell values within one region into an average and a variability range ($\pm 1\sigma$). In the same way, a multigrid cell average of the correlation value resulting from the linear least squares model fit and the importance of the individual factors in these models is calculated. Note that the number of grid cells within such a regional average strongly differs per region and depth (Figure 10). The previously found spatial coherency in these regions warrants the robustness of the results despite the small number of grid cells for which the calculations are done.

This regional analysis reveals that the simulated evolution of flow speeds in the Nordic Seas has a 0.78 correlation to a combined evolution of NSDW and SSDW (Figure 10a). In contrast, the δ^{13}C evolution in the Nordic Seas is not correlated to the evolution of NSDW but is strongly (0.97) related to NH source region δ^{13}C changes. This strong correlation was expected since the source region signal is an average of the surface waters of roughly the same region and the waters in the Nordic Seas are relatively well mixed vertically. Note that the calculated partial correlation of changes in SSDW to the flow speeds in the Nordic Seas does not necessarily imply that SSDW enters the Nordic Seas; this feature will be further discussed in section 4. From the Nordic Seas deep convection regions, deep waters flow into the Atlantic via two main gateways: the Denmark Strait and the Iceland-Scotland Overflow. The evolution of flow speed in these two outflow regions is again dominated by the combined NSDW and SSDW evolution (correlation of 0.94 for both regions; Figures 10b and 10c), and the NH source region δ^{13}C signal also dominates the δ^{13}C evolution (correlations of 0.97 and 0.96, for the Denmark Strait and the Iceland-Scotland Overflow, respectively). We conclude that the evolution of δ^{13}C in the Nordic Seas and near the outflow regions is strongly linked to NH source region
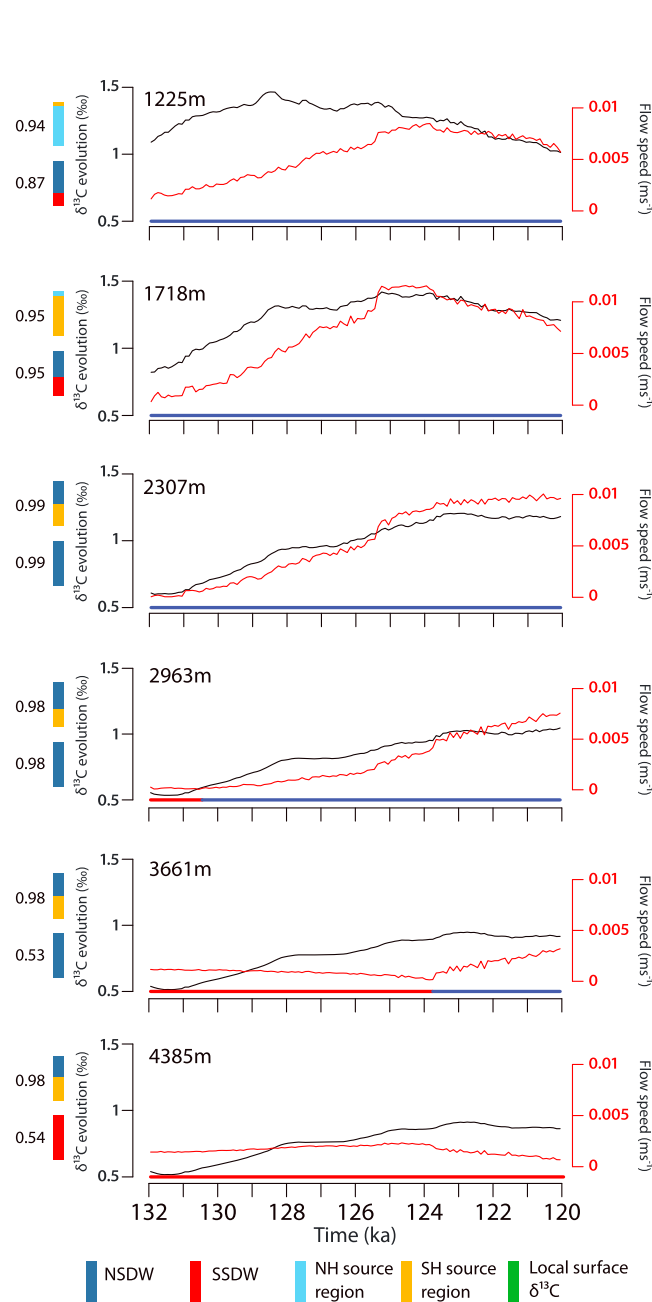
Figure 11. Simulated evolution of δ^{13}C (‰; black) and flow speed (m s^{-1}; red) in single grid cell located in the DWBC close to the Blake Outer Ridge region (27°N and 68°W) for six different depth levels. Shown by the vertical colored bars in front of the figures are the relative importance of the different forcing mechanisms in the calculated best linear fit between the simulated δ^{13}C evolution and the drivers (upper color bar) and the flow speed evolution and the drivers (lower color bar; note that for flow speed only NSDW and SSDW are taken into account in linear correlation model). The resulting best correlation is given in front of the color bars. The horizontal bars in bottom of the individual figures show the predominance through time of NSDW or SSDW (based on a southward or northward flow direction, respectively) at the given depth level.

δ^{13}C changes, while the evolution of flow speeds correlates dominantly with the transport of NSDW. More specifically, the flow speeds in the two overflow regions reveal that deep water formation in the Nordic Seas strongly increased in the period ~130–125 ka and remained almost constant thereafter.

Continuing southward into the Atlantic Ocean, we see that the δ^{13}C evolution at the 1717 m level in the Labrador Sea correlates (0.86) with a mixture of NH and SH source δ^{13}C signals, whereas the flow speed evolution at this depth is not correlated to either NSDW or SSDW (0.29; Figure 10d). A completely different picture emerges at the 2961 m level where both flow speeds and δ^{13}C are highly correlated to NSDW changes. At the 4358 m level, the good correlation between the δ^{13}C evolution and NSDW remains, while it is no longer found for the flow speed evolution. The sudden flow speed increase at the 2961 m level in the Labrador Sea reveals the initiation of deep convection in the Labrador Sea, around 125–124 ka with increasing values thereafter, as it was described in section 2.3 based on changes in the convective layer depth in the Labrador Sea. For the two regions along the path of the DWBC, the midwestern Atlantic and the equatorial western Atlantic (Figures 10e and 10f), we find similarities and dissimilarities, both between the two DWBC sites and between the patterns described for the Labrador Sea region. Especially in the equatorial western Atlantic, the flow speed evolution is highly correlated to changes in NSDW and SSDW transport, with the former dominating the 2961 m level and the latter the 1717 and 4358 m levels. The δ^{13}C evolution is again mostly related to changes in NSDW transport and SH source region δ^{13}C changes. At the 2961 m level the δ^{13}C evolution is mostly explained by NSDW changes, and at the 1717 and 4358 m levels SH source region δ^{13}C changes explain most of the simulated δ^{13}C evolution.
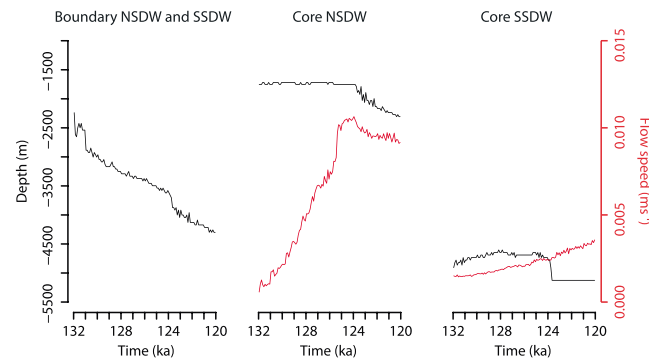
Figure 12. Simulated changes in the depth (m) of the cores of NSDW, SSDW, and the boundary between the two water masses in a single grid cell in the DWBC close to the Blake Outer Ridge region (27°N and 68°W; black lines). The boundary and the cores of the different water masses are based on, respectively, the zero, maximum southward, and maximum northward meridional velocities (between 1200 and 5500 m depth). Also shown is the evolution of flow speed (m s^{-1}; red lines) at the depth of the flow speed-based cores of NSDW and SSDW. Note that the model only has seven unevenly spaced levels in the 1200–5500 m domain. For the presented values, interpolated vertical velocity profiles have been used using the lowess technique.

Interestingly, the correlation of flow speeds with either NSDW or SSDW is much higher for the equatorial western Atlantic sites compared to the low correlation at the midlatitude western Atlantic sites (Figures 10e and 10f), indicating a more regional and complex flow speed signal in the midwestern Atlantic.

3.4. Local Scale

Our results so far indicate that the simulated flow speed evolution can, at specific sites, be strongly linked to the evolution of NSDW but also reveal a much more complex and seemingly uncorrelated signal. This result could imply a purely local forcing of the flow speeds and thus no link to large-scale oceanographic changes or a more complex reflection of such circulation changes. For a better understanding of these local complexities, we zoom in on the smallest scale possible within a climate model and closest to the spatial scale of a sediment core, the vertical water column of a single grid cell. We focus on a grid cell in the midlatitude part of the DWBC (Figure 11; see Figure 1 for the geographical position) that, in the model, has a distinct vertical water mass structure, with a core of NSDW overlying a core of SSDW. Furthermore, we will explore the vertical evolution of the depth and thickness of the two main water masses, NSDW and SSDW, and the boundary between the two (Figure 12). Sensitivity experiments in which the analysis is performed for a number of different single grid cells in the path of the DWBC (not shown) indicate that the following results are largely independent of the choice of this particular grid cell. We note that the grid cell scale (3° longitude by 3° latitude) is still orders of magnitude larger than local processes (as small as kilometer scales) that impact SS values measured in sediment cores. However, arguably SS reconstructions retrieved from the right sedimentary settings provide information on flow speed changes on spatial scales that are comparable to the model grid cell scale [*Thornalley et al.*, 2013a].

During the period ~131–124 ka, δ^{13}C values in the DWBC increase steadily at most levels below ~2000 m as a result of the increasing formation of deep water in the Nordic Seas (Figure 11). During the same period, flow speeds also increase, except at the 3661 and 4385 m levels. The deepest level is bathed by SSDW (Figure 11), and the near-zero flow speed changes simulated during this first period at 4385 m result from a small increase in the flow speed in the core of SSDW that is compensated by a deepening of the SSDW core (Figure 12). The same processes are at play at the 3661 m level (Figure 11), but as this level is closer to the boundary between the two water masses, the net result is a flow speed decrease.

Between ~124 and 120 ka, deep water formation in the Nordic Seas stabilizes while deep convection starts in the Labrador Sea and keeps on invigorating until the end of the simulation at 120 ka. Interestingly, the resulting δ^{13}C evolution in the DWBC at the levels affected by NSDW changes (~2000–4000 m) do not reveal any changes between 124 and 120 ka (Figure 11). This can be explained by a compensation of the deepening of the core of NSDW (Figure 12) by the strongly decreasing δ^{13}C values in the NH source region (Figure 4). Thus, according to this simulation, the initiation and invigoration of deep convection in the Labrador Sea does not result in apparent δ^{13}C changes in the DWBC. However, the changes in flow speeds at the different depth levels reveal distinct trends for the ~124–120 ka period (Figure 11). These trends also contrast with the first part of the LIG (131–124 ka). As the core of NSDW moves away from the 1225 and 1718 m levels (Figure 12), flow speeds decrease at these levels. At the 2307 m level, flow speeds remain almost constant, which is a combined signal of small decreases in the flow speeds in the core of the NSDW and the closing in of

the NSDW core toward this specific location. This latter effect is stronger at the next depth level (2963 m) where flow speeds show a strong increase between 124 and 120 ka and even stronger at the 3661 m level that is now bathed by NSDW (Figure 11). Bathed by SSDW with a core that is moving toward even deeper waters, the deepest level exhibits again decreasing flow speeds (Figure 11).

4. Discussion

The presented results indicate that simulated time series of flow speeds and $\delta^{13}C$ from different regions can be linked to a single driving factor or a combination of a few factors: NSDW and SSDW for flow speeds, and NSDW, NH source region, and SH source region $\delta^{13}C$ changes for the $\delta^{13}C$ evolution. However, these factors are not necessarily the same for flow speeds and $\delta^{13}C$. Moreover, the simulated $\delta^{13}C$ evolution appears to be coherent over large spatial scales whereas flow speeds tend to show coherent patterns in a few regions only. Flow speed and $\delta^{13}C$ time series from a single site can thus either be correlated to one another or not. Finally, despite the apparent local nature of the flow speed evolution, investigating their evolution in specific regions like the DWBC can yield important information on changes in the vertical water mass structure that cannot be obtained from $\delta^{13}C$ time series alone.

In the following, we first discuss the limitations of using a linear correlation model to investigate the main factors driving simulated changes in flow speeds and $\delta^{13}C$. We then examine whether the detailed description of deep-ocean circulation variables such as flow speed and $\delta^{13}C$, as shown within the theoretical framework of a climate model simulation, can help explain proxy-based reconstructions. This section ends with a description of the possible limitations of the climate model, scenario, and initial conditions that were used and how they might explain some of the model-data mismatches.

4.1. Limitations of the Applied Linear Correlation Model

To provide insight into the simulated spatial and temporal evolution of flow speeds and $\delta^{13}C$ during a period that is characterized by a large increase in the strength of the AMOC, we calculated least squares residual fits between the simulated parameter and a linear combination of the predetermined main driving factors. This is a relatively simplistic method that revealed many of the well-known Atlantic deep-ocean water mass characteristics. However, there are several important limitations to the approach: (i) the method implies that the relative contribution of the different driving factors for a single grid cell is constant in time. This restriction is unlikely to be valid. (ii) The different driving factors are assumed to be independent, an unlikely condition in such a complex system as the Earth's climate. We find, for instance, a correlation of 0.8 between the evolution of NSDW and the SH $\delta^{13}C$ source region signal and a correlation of -0.9 between the SH $\delta^{13}C$ source region signal and the mean surface $\delta^{13}C$ signal in the Atlantic basin (Table S3 in the supporting information). Whether or not these high correlations between the different driving factors occur by chance or because they are in turn linked to a common forcing like changes in insolation is not easily assessed because of the complex nature of the climate system. (iii) It cannot be ruled out that the described least squares residuals fits are nonunique results, implying that a different combination of driving factors potentially yields a very similar, though slightly lower, correlation factor.

The limitations described above could explain some of the apparent good $\delta^{13}C$ correlations that have been found for cases in which a physical explanation is lacking. Two such cases are the described correlation between the $\delta^{13}C$ evolution in the high SH latitudes and the $\delta^{13}C$ changes within the NH source region or the high correlation between the simulated $\delta^{13}C$ evolution in NH latitudes as high as 55°N and $\delta^{13}C$ changes in the SH source region (Figure 6). However, another possibility is that the calculated correlations are not caused by limitations in the applied methodology but by physical mechanisms that we do not understand yet. For instance, there could be an atmospheric teleconnection between the NH source region and the high SH latitudes, which is not investigated in this study. An in-depth study of this topic is potentially highly rewarding.

4.2. DWBC Case Study of Model-Data Comparison

To investigate if our model-based findings can help disentangle proxy-based SS and $\delta^{13}C$ time series, we performed a preliminary model-data comparison. If successful, it will also allow us to determine the validity of the enforced AMOC evolution. To this end, we compiled a total of five locations from a NH midlatitude section of the DWBC (between 28°N–32°N and 73°W–76°W and between 2584 and 4758 m depth) that
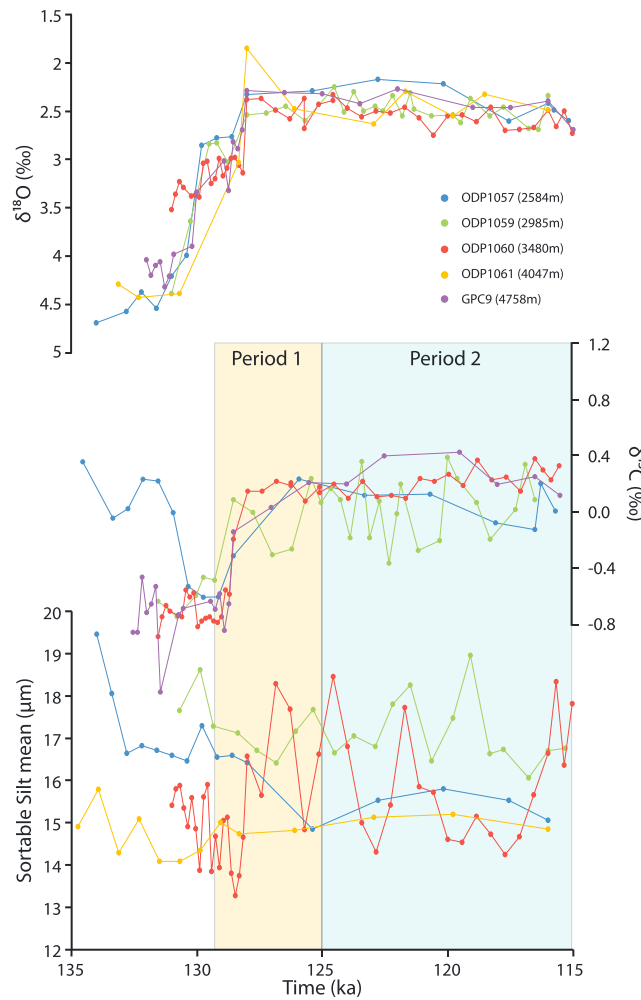
Figure 13. The proxy-based reconstructions of (middle) DWBC δ^{13}C (‰) and (bottom) flow speed (m s^{-1}) and (top) the aligned δ^{18}O curves (‰) used to construct the age model by tuning them to the benthic δ^{18}O stratigraphy described in *Shackleton et al.* [2002, 2003] following the rational described by *Hodell et al.* [2009]. Results are shown for a compilation of five records from the Blake-Bahama Outer Ridge region in the vicinity of the DWBC. Included are δ^{13}C records from ODP1057, ODP1059, ODP1060, and GPC9 and sortable silt records from ODP1057, ODP1059, ODP1060, and ODP1061. Also shown are the two periods defined in the manuscript (~129–125 ka and 125–115 ka) that are based on the presence or absence of large δ^{13}C changes common to all records. The tie points used to synchronize the different records are listed in Table S2.

present reconstructed δ^{13}C and SS records for the period of interest. The DWBC was chosen for the model-data comparison because of the high proxy data availability from a relatively small region and because our model results indicate that throughout most of the DWBC region changes in flow speed and δ^{13}C are highly correlated to large-scale driving factors. Three of the compiled records contain both ocean circulation variables (namely ODP1057, ODP1059, and ODP1060), and the other two contain either δ^{13}C (GPC9) or sortable silt (ODP1061; see Table S1 for additional information and references). Oxygen and carbon isotopic compositions were measured on *Cibicidoides* species in cores ODP1057, ODP1059, and GPC9 and mixed *Cibicidoides* and *Uvigerina* species in core ODP1060 over the LIG. Typical corrections of +0.64‰ and +0.70‰ (i.e., within the error of the correction of +0.85 ± 0.48‰ used by *Oliver et al.*, 2010) were applied to *Cibicidoides* δ^{18}O values and *Uvigerina* δ^{13}C values, respectively. All benthic foraminiferal δ^{18}O records were aligned (Figure 13) and placed on the stratigraphy proposed by *Shackleton et al.* [2002, 2003], following the approach described in *Hodell et al.* [2009]. Defined tie points are given in Table S2. Alignment uncertainties mostly depend on the resolution of benthic δ^{18}O records and range between 0.4 and 1.6 ky (in cores ODP 1060 and 1061, respectively). Although the evolution of δ^{18}O may not be synchronous at different depths, in particular across Terminations [*Lisiecki and Raymo*, 2009; *Waelbroeck et al.*, 2011; *Ganopolski*

and Roche, 2009] no apparent offset could be evidenced between benthic δ^{18}O records from different water depths within the North Atlantic throughout Termination II and the LIG [*Govin et al.*, 2012]. Absolute dating uncertainties reach up to 2–3 ky in the tuning approach of *Shackleton et al.* [2002, 2003]. However, the most important limitation of the following model-data comparison is likely the low temporal resolution of most sortable silt records, especially in cores ODP1059 and ODP1061. Therefore, we consider the presented model-data comparison only a test case that will hopefully stimulate future research along these lines. Moreover, because of biases and uncertainties in the alignment of simulated and reconstructed flow speed and δ^{13}C time series in both time and depth, we deemed it inappropriate to present the model-data comparison in a single figure.

The reconstructed δ^{13}C time series for the DWBC show LIG evolutions similar to those simulated by the model: a first period of increasing values and a plateau with values similar to present day, referred to as

periods 1 and 2, respectively, in Figure 13. However, the magnitude of the reconstructed +0.7‰ δ^{13}C increase in period 1 (~129–125 ka) is not matched by the model results. Period 1 includes part of the late deglacial period, as indicated by the onset of the LIG benthic δ^{18}O plateau (reflecting at first order the onset of high sea levels) occurring here at ~128 ka. Deglacial δ^{13}C changes have been attributed to a range of mechanisms including a reinvigoration of the AMOC, brine-induced stratification, stratification-dependent diffusion, iron fertilization, carbon compensation, and terrestrial carbon reservoir changes [*Bouttes et al.*, 2011]. Because only the reinvigoration of the AMOC and changes in the terrestrial carbon reservoir are included in the performed climate model experiment, simulated δ^{13}C changes cannot perfectly match the magnitude of reconstructed δ^{13}C changes. In addition, the shift from relatively low to relatively high δ^{13}C values is more rapid in the reconstructions (~3 ky) than in the simulation (~8 ky). This model-data mismatch could signal an important role for one of the missing deglacial δ^{13}C driving mechanisms listed earlier, or it could indicate that the imposed AMOC evolution is incomplete. To investigate whether the reconstructed (~129–125 ka) positive shifts in δ^{13}C relates to a strengthening of the AMOC, we extend this model-data comparison to include simulated flow speeds and reconstructed SS values, which can provide complementary information.

For the model-data comparison of flow speeds, we focus again on the changes within the two LIG periods defined above. Based on the model findings, we would expect all SS records to show increasing values during the first part of the LIG. This appears to be true for the two deeper cores (3480 and 4047 m). However, the two shallower cores reveal either no trend (2985 m) or a decreasing trend (2584 m). During the second part of the LIG, the simulated flow speed changes resulting from the initiation and invigoration of Labrador Sea convection cause a deepening of the cores of both NSDW and SSDW and concurrent increase (decrease) in flow speed depending on whether the depth level is below (above) the core of the respective water mass. If a similar vertical water mass structure is assumed in model and data, flow speed increases are expected at all proxy record depth level. Flow speeds at 2584, 2985, and 4047 m are slightly increasing throughout this period, but both the changes and the temporal resolution are rather small. Flow speed changes at the 3480 m level are even harder to interpret due to large fluctuations.

Based on the presented preliminary model-data comparison for LIG flow speed and δ^{13}C changes in the midlatitude part of the DWBC, it is not possible to determine the causes of the model-data mismatches: limited number of proxy records and low temporal resolution, coarse resolution, and simplified physics of the *i*LOVECLIM model and the imposed climate model scenario and initial conditions. The latter causes of uncertainty will be discussed in the following section.

4.3. Limitations of the Applied Climate Model, Scenario, and Initial Conditions

Several interesting mismatches observed between the presented model experiment and proxy-based findings can partly explain why a model-data comparison on the scale presented here needs a very careful evaluation. As a possible result of the coarse resolution of the model, the simulated boundary between the NSDW core and SSDW core may be too shallow. Proxy data indeed suggest the presence of NSDW (characterized by high δ^{13}C values) down to 4.6 km during the latter interval of the LIG (Figure 13), whereas the model shows that the boundary between NSDW and SSDW descends from ~3.3 to 4.3 km between 128 and 120 ka (Figure 12). This model bias connects to the too low deep-ocean temperatures described for the comparison of the *i*LOVECLIM results and present-day observations (section 2.2). Another model bias, potentially connected to the low spatial resolution, is the mismatch in the direction of flow of SSDW. In reality, both NSDW and SSDW flow southward in the region of the DWBC under consideration: SSDW enters the eastern North American Basin and then circulates back around Bermuda Rise and becomes incorporated in the southward flowing DWBC [*Weatherly and Kelley*, 1984]. As a consequence, there is in reality no level of no motion between both water masses. Any climate model, no matter the resolution, will have these type of biases, but if the comparison of model and data is done carefully, such biases do not prevent using low-resolution climate models paleoceanographic studies.

Two additional aspects of the model-data comparison related to the imposed initial conditions and the imposed freshwater forcing remain to be elucidated. The first is related to the reconstructed flow speed and δ^{13}C evolution at 2584 m before ~128 ka. Before ~133 ka high flow speed and δ^{13}C values (Figure 13) might be related to a fast flowing and well-ventilated Glacial North Atlantic Intermediate Water bathing the site [e.g., *Thornalley et al.*, 2013b]. A deglacial decrease in δ^{13}C around 132 ka (possibly due to meltwater input; *Oppo et al.*, 1997) marks the presence of a poorly ventilated water mass at the site, probably of

southern origin (SSDW). Thereafter, the increase in δ^{13}C values suggests the presence of well-ventilated NSDW at 2584 m from 128 ka on, in line with a strengthening of the AMOC toward a present-day-like situation at the end of the penultimate deglaciation. In parallel, the gradual decrease in SS values may reflect the deepening of the core of NSDW. Despite the low resolution of the records, this example illustrates the complementarities of benthic δ^{13}C and SS records as tracers of deep-ocean circulation changes and highlights the need to combine both tracers in future paleoclimate reconstructions and simulations. Deep water changes proposed here at ~2500 m could be verified in future simulations, in which the model is initialized from a "glacial" rather than a nearly collapsed AMOC state, as is presented here. The second aspect of the model-data comparison that is possibly associated with the imposed freshwater forcing relates to the formation of deep waters in the Labrador Sea. In the presented simulation, convection in the Labrador Sea is initially absent and starts between 126 and 124 ka (see Figures 3 and 4). This causes a rapid increase in the flow speeds in the Labrador Sea at 2961 m depth (Figure 10) and a deepening of the NSDW core in the DWBC region (Figure 11). This is in contrast with the proxy-based interpretation of *Evans et al.* [2007], who explain the decrease in SS in ODP1057 (2584 m; Figure 13) as an indication of a decrease in the production of Labrador Sea Water (LSW) that at present-day bathes this site. The evolution of LSW production during the LIG is still debated [*Hillaire-Marcel et al.*, 2001; *Rasmussen et al.*, 2003], and the presented results cannot provide an answer but can hopefully initiate a new line of research that can shed light on this matter.

Overall, because of the lack of a general agreement between the simulated and reconstructed flow speed evolutions in the DWBC, we currently cannot determine whether the described agreement between the large-scale simulated and reconstructed δ^{13}C evolution resulted from a common driving factor, namely, changes in the AMOC, or is a mere coincidence. Nevertheless, this preliminary model-data comparison, which integrates for the first time two distinct tracers of the deep-ocean circulation (δ^{13}C and SS), highlights the complementarity of both tracers in paleoclimate reconstructions (in terms of, e.g., position versus intensity of water masses) and the need for developing such multiproxy approaches in future LIG studies.

5. Conclusions

We have presented a first analysis of the simulated impact of imposed multimillennial AMOC changes, from shut down to weakened and finally to a present-day-like state, on the evolution of flow speeds and δ^{13}C in the deep Atlantic Ocean in the *i*LOVECLIM model. The final aim is to move toward more direct model-data comparisons of past deep-ocean circulation changes. For this reason, we focus on simulating the AMOC evolution during the LIG period as a case study. We correlated the simulated flow speed evolution per grid cell to a linear combination of changes in NSDW and SSDW transport, and the simulated δ^{13}C evolution to changes in NSDW and SSDW transport, changes in the NH source region δ^{13}C signal, the SH source region δ^{13}C signal, and the local surface water δ^{13}C signal. By beginning the analysis on the basin scale and identifying regions that show spatial coherence to the large-scale driving factors, we are able to investigate progressively circulation changes on smaller spatial scales in these specific regions.

The flow speed evolution in general shows little spatial coherency and highest correlations to NSDW as large-scale driving factor in regions that are bathed by NADW and more specifically in the DWBC. In these regions, changes in flow speeds at different depth levels can provide important complementary information on the vertical migration of water masses and allows us to differentiate between the initiation of convection in the Nordic Seas and in the Labrador Sea, whereas this information could not be gained from the evolution of δ^{13}C alone. Contrary to flow speeds, the simulated evolution of δ^{13}C reveals spatially coherent correlation over large parts of the deep Atlantic. The δ^{13}C changes in the areas bathed by NADW are again closely correlated to NSDW changes, while, further north, the δ^{13}C evolution in the Nordic Seas and the overflow regions are dominated by changes in the NH source regions signal. Finally, the δ^{13}C evolution in the northward flowing water masses identified as AABW and AAIW are driven by changes in the SH source regions δ^{13}C signal. Overall, we show that the evolution of flow speeds and δ^{13}C can provide different but complementary information on the LIG evolution of the deep Atlantic circulation. Moreover, changes in the production and deep waters and the strength of the AMOC are not necessarily recorded by seawater δ^{13}C, stressing the need for more paleoclimate studies combining both tracers. It cannot be ruled out that some of the results presented here are model dependent, especially because of model differences in, e.g., the exact location and depths of water masses present within the Atlantic basin.

The preliminary model-data comparison presented for a midlatitude section of the DWBC is not straightforward and reveals mismatches that remain difficult to elucidate. It is so far not possible to assess whether the observed mismatches are caused by the limitations of the LIG proxy records in terms of dating errors and low temporal resolutions, inherent to the use of a low-resolution climate model or the result of the imposed AMOC evolution or caveats in the initial conditions. Nevertheless, this first example illustrates how the combination of both flow speeds and $\delta^{13}C$ in the framework of a model-data comparison, if cautiously performed, could yield new insights and details on the multimillennial evolution of North Atlantic deep-ocean circulation.

In conclusion, we strongly encourage future model-data comparisons of flow speeds and $\delta^{13}C$ as a tool to gain a deeper understanding of past multimillennial changes in the deep-ocean circulation. Investigating more recent periods characterized by NH freshwater input and for which high-resolution records are available (e.g., the Younger Dryas) could help disentangle the limitations of proxy records versus climate models. Additional model simulations would also be required to understand some intriguing features observed in this study, such as the lack of a NSDW-driven $\delta^{13}C$ signal in the Nordic Seas and overflow regions, a NH source region $\delta^{13}C$ signal in SH high latitudes, and the absence of signals driven by the SSDW transport throughout the Atlantic basin.

References

Alley, R. B., P. A. Mayewski, T. Sowers, M. Stuiver, K. C. Taylor, and P. U. Clark (1997), Holocene climatic instability: A prominent, widespread event 8200 yr ago, *Geology*, *25*, 483–486, doi:10.1130/0091-7613(1997)025<0483.

Alley, R. B., et al. (2010), History of the Greenland Ice Sheet: Paleoclimatic insights, *Quat. Sci. Rev.*, *29*(15–16), 1728–1756, doi:10.1016/j.quascirev.2010.02.007.

Bakker, P., C. J. Van Meerbeeck, and H. Renssen (2012), Sensitivity of the North Atlantic climate to Greenland Ice Sheet melting during the Last Interglacial, *Clim. Past*, *8*, 995–1009, doi:10.5194/cp-8-995-2012.

Bakker, P., H. Renssen, and C. J. Van Meerbeeck (2013a), Early Last Interglacial Greenland ice sheet melting and a sustained period of meridional overturning weakening: A model analysis of the uncertainties, *Clim. Dyn.*, *43*(3–4), 1025–1039, doi:10.1007/s00382-013-1935-1.

Bakker, P., et al. (2013b), Last Interglacial temperature evolution—A model inter-comparison, *Clim. Past.*, *9*, 605–619, doi:10.5194/cp-9-605-2013.

Bauch, H. A. (2013), Interglacial climates and the Atlantic meridional overturning circulation: Is there an Arctic controversy?, *Quat. Sci. Rev.*, *63*, 1–22, doi:10.1016/j.quascirev.2012.11.023.

Berger, A. L. (1978), Long-term variations of caloric insolation resulting from the Earth's orbital elements, *Quat. Res.*, *9*(2), 139–167, doi:10.1016/0033-5894(78)90064-9.

Bouttes, N., D. M. Roche, and D. Paillard (2009), Impact of strong deep ocean stratification on the glacial carbon cycle, *Paleoceanography*, *24*, PA3203, doi:10.1029/2008PA001707.

Bouttes, N., D. Paillard, and D. M. Roche (2010), Impact of brine-induced stratification on the glacial carbon cycle, *Clim. Past*, *6*, 575–589, doi:10.5194/cp-6-575-2010.

Bouttes, N., D. Paillard, D. M. Roche, V. Brovkin, and L. Bopp (2011), Last Glacial Maximum CO$_2$ and $\delta^{13}C$ successfully reconciled, *Geophys. Res. Lett.*, *38*, L02705, doi:10.1029/2010GL044499.

Bouttes, N., D. M. Roche, V. Mariotti-Epelbaum, and L. Bopp (2014), Including a full carbon cycle into the *i*LOVECLIM model (v1.0), *Geosci. Model. Dev. Discuss.*, *7*, 3937–3984, doi:10.5194/gmdd-7-3937-2014.

Boyer, T. P., J. I. Antonov, O. K. Baranova, H. E. Garcia, D. R. Johnson, R. A. Locarnini, A. V. Mishonov, D. Seidov, I. V. Smolyar, and M. M. Zweng (2009), in *World Ocean Database 2009, vol. 1, Introduction, NOAA Atlas NESDIS*, vol. 66, edited by S. Levitus, 219 pp., NOAA, Silver Spring, Md.

Brovkin, V., J. Bendtsen, M. Claussen, A. Ganopolski, C. Kubatzki, V. Petoukhov, and A. Andreev (2002), Carbon cycle, vegetation, and climate dynamics in the Holocene: Experiments with the CLIMBER-2 model, *Global Biogeochem. Cycles*, *16*(4), 1139, doi:10.1029/2001GB001662.

Brovkin, V., A. Ganopolski, D. Archer, and S. Rahmstorf (2007), Lowering of glacial atmospheric CO$_2$ in response to changes in oceanic circulation and marine biogeochemistry, *Paleoceanography*, *22*, PA4202, doi:10.1029/2006PA001380.

Caley, T., and D. M. Roche (2013), $\delta^{18}O$ water isotope in the *i*LOVECLIM model (version 1.0)—Part 3: A palaeo-perspective based on present-day data–model comparison for oxygen stable isotopes in carbonates, *Geosci. Model Dev.*, *6*, 1505–1516, doi:10.5194/gmd-6-1505-2013.

CAPE Members (2006), Last Interglacial Arctic warmth confirms polar amplification of climate change, *Quat. Sci. Rev.*, *25*(13–14), 1383–1400, doi:10.1016/j.quascirev.2006.01.033.

Craig, H. (1957), Isotopic standards for carbon and oxygen and correction factors for mass-spectrometric analysis of carbon dioxide, *Geochim. Cosmochim. Acta*, *12*(1–2), 133–149, doi:10.1016/0016-7037(57)90024-8.

de Vernal, A., and C. Hillaire-Marcel (2008), Natural variability of Greenland climate, vegetation, and ice volume during the past million years, *Science*, *320*, 1622–1625, doi:10.1126/science.1153929.

Duplessy, J. C., A. W. H. Bé, and P. L. Blanc (1981), Oxygen and carbon isotopic composition and biogeographic distribution of planktonic foraminifera in the Indian Ocean, *Palaeogeogr. Palaeoclimatol. Palaeoecol.*, *33*, 9–46, doi:10.1016/0031-0182(81)90031-6.

Dutton, A., and K. Lambeck (2012), Ice volume and sea level during the Last Interglacial, *Science*, *337*, 216–219, doi:10.1126/science.1205749.

Ellison, C. R. W., M. R. Chapman, and I. R. Hall (2006), Surface and deep ocean interactions during the cold climate event 8200 years ago, *Science*, *312*(5782), 1929–1932, doi:10.1126/science.1127213.

Evans, H. K., I. R. Hall, G. G. Bianchi, and D. W. Oppo (2007), Intermediate water links to Deep Western Boundary Current variability in the subtropical NW Atlantic during marine isotope stages 5 and 4, *Paleoceanography*, *22*, PA3209, doi:10.1029/2006PA001409.

Fronval, T., J. Eystein, H. Haflidason, and H.-P. Sejrup (1998), Variability in surface and deep water conditions in the Nordic Seas during the Last Interglacial period, *Quat. Sci. Rev.*, *17*, 963–985, doi:10.1130/G20901.1.

Galaasen, E. V., U. S. Ninnemann, N. Irvalı, H. F. Kleiven, Y. Rosenthal, C. Kissel, and A. Hodell (2014), Rapid reductions in North Atlantic Deep Water during the peak of the Last Interglacial period, *Science*, *343*(6175), 1129–1132, doi:10.1126/science.1248667.

Ganopolski, A., and D. M. Roche (2009), On the nature of lead-lag relationships during glacial-interglacial climate transitions, *Quat. Sci. Rev.*, *28*(27–28), 3361–3378, doi:10.1016/j.quascirev.2009.09.019.

Goosse, H., and T. Fichefet (1999), Importance of ice-ocean interactions for the global ocean circulation: A model study, *J. Geophys. Res.*, *104*(C10), 23,337–23,355, doi:10.1029/1999JC900215.

Goosse, H., et al. (2010), Description of the Earth system model of intermediate complexity LOVECLIM version 1.2, *Geosci. Model. Dev.*, *3*(1), 309–390, doi:10.5194/gmd-3-603-2010.

Gordon, A. L. (1986), Interocean exchange of thermocline water, *J. Geophys. Res.*, *91*, 5037–5046, doi:10.1029/JC091iC04p05037.

Govin, A., et al. (2012), Persistent influence of ice sheet melting on high northern latitude climate during the early Last Interglacial, *Clim. Past*, *8*, 483–507, doi:10.5194/cp-8-483-2012.

Hillaire-Marcel, C., A. de Vernal, G. Bilodeau, and A. J. Weaver (2001), Absence of deep-water formation in the Labrador Sea during the Last Interglacial period, *Nature*, *410*(6832), 1073–1077, doi:10.1038/35074059.

Hodell, D. A., E. K. Minth, J. H. Curtis, I. N. McCave, I. R. Hall, J. E. T. Channell, and C. Xuan (2009), Surface and deep-water hydrography on Gardar Drift (Iceland Basin) during the Last Interglacial period, *Earth Planet. Sci. Lett.*, *288*(1–2), 10–19, doi:10.1016/j.epsl.2009.08.040.

Jones, P. D., et al. (2009), High-resolution palaeoclimatology of the last millennium: A review of current status and future prospects, *Holocene*, *19*, 3–49, doi:10.1177/0959683608098952.

Kleiven, H. F., C. Kisse, C. Lai, U. S. Ninnemann, T. O. Richter, and E. Cortijo (2008), Reduced North Atlantic deep water coeval with the glacial Lake Agassiz freshwater outburst, *Science*, *319*, 60–64, doi:10.1126/science.1148924.

Koerner, R. M. (1989), Ice core evidence for extensive melting of the Greenland ice sheet in the Last Interglacial, *Science*, *244*(4907), 964–968.

Kopp, R. E., F. J. Simons, J. X. Mitrovica, A. C. Maloof, and M. Oppenheimer (2009), Probabilistic assessment of sea level during the Last Interglacial stage, *Nature*, *462*, 863–867, doi:10.1038/nature08686.

Kroopnick, P. M. (1985), The distribution of ^{13}C of ΣCO_2 in the world oceans, *Deep Sea Res., Part A*, *32*, 57–84, doi:10.1016/0198-0149(85)90017-2.

Kuhlbrodt, T., A. Griesel, M. Montoya, A. Levermann, M. Hofmann, and S. Rahmstorf (2007), On the driving processes of the Atlantic meridional overturning circulation, *Rev. Geophys.*, *45*, RG2001, doi:10.1029/2004RG000166.

Lisiecki, L. E., and M. E. Raymo (2009), Diachronous benthic δ^{18}O responses during late Pleistocene terminations, *Paleoceanography*, *24*, PA3210, doi:10.1029/2009PA001732.

Loulergue, L., A. Schilt, R. Spahni, V. Masson-Delmotte, T. Blunier, B. Lemieux, J. M. Barnola, D. Raynaud, T. F. Stocker, and J. Chappellaz (2008), Orbital and millennial-scale features of atmospheric CH_4 over the past 800,000 years, *Nature*, *453*, 383–386, doi:10.1038/nature06950.

Lund, D. C., J. Lynch-Stieglitz, and W. B. Curry (2006), Gulf Stream density structure and transport during the past millennium, *Nature*, *444*, 601–604, doi:10.1038/nature05277.

Lunt, D. J., et al. (2013), A multi-model assessment of Last Interglacial temperatures, *Clim. Past*, *9*, 699–717, doi:10.5194/cp-9-699-2013.

Luthi, D., et al. (2008), High-resolution carbon dioxide concentration record 650,000–800,000 years before present, *Nature*, *453*, 379–382, doi:10.1038/nature06949.

Marshall, J., and F. Schott (1999), Open-ocean convection: Observations, theory and models, *Rev. Geophys.*, *37*(1), 1–64, doi:10.1029/98RG02739.

McCartney, M. S., and L. D. Talley (1984), Warm-to-cold water conversion in the northern North Atlantic Ocean, *J. Phys. Oceanogr.*, *14*, 922–935, doi:10.1175/1520-0485(1984)014<0922:WTCWCI>2.0.CO;2.

McCave, I. N., and I. R. Hall (2006), Size sorting in marine muds; processes, pitfalls, and prospects for paleoflow-speed proxies, *Geochem. Geophys. Geosyst.*, *7*, Q10N05, doi:10.1029/2006GC001284.

McCave, I. N., B. Manighetti, and S. G. Robinson (1995), Sortable silt and fine sediment size/composition slicing: Parameters for palaeocurrent speed and palaeoceanography, *Paleoceanography*, *10*, 593–610, doi:10.1029/94PA03039.

McKay N. P., J. T. Overpeck, and B. L. Otto-Bliesner (2011), The role of ocean thermal expansion in Last Interglacial sea level rise, *Geophys. Res. Lett.*, *38*, L14605, doi:10.1029/2011GL048280.

NEEM community members (2013), Eemian interglacial reconstructed from a Greenland folded ice core, *Nature*, *493*(7433), 489–494, doi:10.1038/nature11789.

Nicholl, J. A. L., D. A. Hodell, B. D. A. Naafs, C. Hillaire-Marcel, J. E. T. Channell, and O. E. Romero (2012), A Laurentide outburst flooding event during the Last Interglacial period, *Nat. Geosci.*, *5*, 901–904, doi:10.1038/ngeo1622.3.

Oliver, K. I. C., B. A. A. Hoogakker, S. Crowhurst, G. M. Henderson, R. E. M. Rickaby, N. R. Edwards, and H. Elderfield (2010), A synthesis of marine sediment core δ^{13}C data over the last 150 000 years, *Clim. Past*, *6*(5), 645–673, doi:10.5194/cp-6-645-2010.

Oppo, D. W., M. Horowitz, and S. J. Lehman (1997), Marine core evidence for reduced deep water production during Termination II followed by a relatively stable substage 5e (Eemian), *Paleoceanography*, *12*, 51–63, doi:10.1029/96PA03133.

Oppo, D. W., J. F. McManus, and J. Cullen (2006), Evolution and demise of the Last Interglacial warmth in the subpolar North Atlantic, *Quat. Sci. Rev.*, *25*, 3268–3277, doi:10.1016/j.quascirev.2006.07.006.

Opsteegh, J. D., R. J. Haarsma, F. M. Selten, and A. Kattenberg (1998), ECBILT: A dynamic alternative to mixed boundary conditions in ocean models, *Tellus, Ser. A*, *50*(3), 348–367, doi:10.1034/j.1600-0870.1998.t01-1-00007.x.

Otto-Bliesner, B. L., S. J. Marshall, J. T. Overpeck, G. H. Miller, and A. Hu (2006), Simulating arctic climate warmth and icefield retreat in the last interglaciation, *Science*, *311*, 1751–1753, doi:10.1126/science.1120808.

Praetorius, S. K., J. F. McManus, D. W. Oppo, and W. B. Curry (2008), Episodic reductions in bottom-water currents since the last ice age, *Nat. Geosci.*, *1*(7), 449–452, doi:10.1038/ngeo227.

Rasmussen, T. L., D. W. Oppo, E. Thomsen, and S. J. Lehman (2003), Deep sea records from the southeast Labrador Sea: Ocean circulation changes and ice-rafting events during the last 160,000 years, *Paleoceanography*, *18*(1), 1018, doi:10.1029/2001PA000736.

Rensson, H., E. Driesschaert, M. F. Loutre, and T. Fichefet (2006), On the importance of initial conditions for simulations of the Mid-Holocene climate, *Clim. Past*, *2*, 91–97, doi:10.5194/cp-2-91-2006.

Roche, D. M. (2013), δ^{18}O water isotope in the *i*LOVECLIM model (version 1.0)—Part 1: Implementation and verification, *Geosci. Model Dev.*, *6*, 1481–1491, doi:10.5194/gmd-6-1481-2013.

Sánchez Goñi, M., et al. (2012), European climate optimum and enhanced Greenland melt during the Last Interglacial, *Geology*, *40*, 627–630, doi:10.1130/G32908.1.

Schilt, A., M. Baumgartner, T. Blunier, J. Schwander, R. Spahni, H. Fischer, and T. F. Stocker (2010), Glacial-interglacial and millennial-scale variations in the atmospheric nitrous oxide concentration during the last 800,000 years, *Quat. Sci. Rev.*, *29*, 182–192, doi:10.1016/j.quascirev.2009.03.011.

Shackleton, N. J. (1977), Carbon-13 in Uvigerina: Tropical rainforest history and the equatorial Pacific carbonate dissolution cycles, in *The Fate of Fossil Fuel CO_2 in the Oceans*, edited by N. R. Anderson and A. Malahoff, pp. 401–427, Plenum Press, New York.

Shackleton, N. J., M. R. Chapman, M. F. Sánchez-Goñi, D. Pailler, and Y. Lancelot (2002), The classic marine isotope substage 5e, *Quat. Res.*, *58*, 14–16, doi:10.1006/qres.2001.2312.

Shackleton, N. J., M. F. Sánchez-Goñi, D. Pailler, and Y. Lancelot (2003), Marine isotope substage 5e and the Eemian interglacial, *Global Planet. Change*, *36*(3), 151–155, doi:10.1016/S0921-8181(02)00181-9.

Solomon, S., D. Qin, M. Manning, Z. Chen, M. Marquis, K. B. Averyt, M. Tignor, and H. L. Miller (Eds.) (2007), *IPCC 2007: Climate Change 2007: The Physical Science Basis. Contribution of Working Group 1 to the Fourth Assessment Report of the Intergovernmental Panel on Climate Change*, 996 pp., Cambridge Univ. Press, Cambridge, U. K., and New York.

Stommel, H. M. (1957), A survey of ocean current theory, *Deep Sea Res.*, *4*(3), 149–184, doi:10.1016/0146-6313(56)90048-X.

Stone, E. J., D. J. Lunt, J. D. Annan, and J. C. Hargreaves (2013), Quantification of the Greenland ice sheet contribution to Last Interglacial sea level rise, *Clim. Past*, *9*(2), 621–639, doi:10.5194/cp-9-621-2013.

Svendsen, J. I., et al. (2004), Late Quaternary ice sheet history of northern Eurasia, *Quat. Sci. Rev.*, *23*, 1229–1271, doi:10.1016/j.quascirev.2003.12.008.

Talley, L. D. (2013), Closure of the global overturning circulation through the Indian, Pacific, and Southern Oceans: Schematics and transports, *Oceanography*, *26*(1), 80–97, doi:10.5670/oceanog.2013.07.

Tarasov, L., and W. R. Peltier (2003), Greenland glacial history, borehole constraints, and Eemian extent, *J. Geophys. Res.*, *108*(B3), 2143, doi:10.1029/2001JB001731.

Thornalley, D. J. R., M. Blaschek, F. J. Davies, S. K. Praetorius, D. Oppo, J. McManus, I. R. Hall, H. F. Kleiven, H. Renssen, and I. N. McCave (2013a), Long-term variations in Iceland–Scotland overflow strength during the Holocene, *Clim. Past*, *9*, 2073–2084, doi:10.5194/cp-9-2073-2013.

Thornalley, D. J. R., S. Barker, J. Becker, I. R. Hall, and G. Knorr (2013b), Abrupt changes in deep Atlantic circulation during the transition to full glacial conditions, *Paleoceanography*, *28*, 253–262, doi:10.1002/palo.20025.

Turney, C. S. M., and R. T. Jones (2010), Does the Agulhas Current amplify global temperatures during super-interglacials?, *J. Quat. Sci.*, *25*(6), 839–843, doi:10.1002/jqs.1423.

Waelbroeck, C., L. C. Skinner, L. Labeyrie, J. C. Duplessy, E. Michel, N. Vazquez Riveiros, J. M. Gherardi, and F. Dewilde (2011), The timing of deglacial circulation changes in the Atlantic, *Paleoceanography*, *26*, PA3213, doi:10.1029/2010PA002007.

Wanner, H., et al. (2008), Mid- to Late Holocene climate change: An overview, *Quat. Sci. Rev.*, *27*, 1791–1828, doi:10.1016/j.quascirev.2008.06.013.

Weatherly, G. L., and E. A. Kelley (1984), Two views of the cold filament, *J. Phys. Oceanogr.*, *15*, 68–81, doi:10.1175/1520-0485(1985)015<0068:TVOTCF>2.0.CO;2.